UCRL-11180

University of California

Ernest O. Lawrence
Radiation Laboratory

PION-PROTON ELASTIC SCATTERING IN THE ENERGY RANGE 300 TO 700 MeV

Berkeley, California

UCRL-11180
UC-34 Physics
TID-4500 (24th Ed.)

UNIVERSITY OF CALIFORNIA
Lawrence Radiation Laboratory
Berkeley, California

AEC Contract No. W-7405-eng-48

PION-PROTON ELASTIC SCATTERING IN THE ENERGY RANGE 300 TO 700 MeV

Philip M. Ogden

(Ph.D. Thesis)

February 20, 1964

Printed in USA. Price $2.25. Available from the
Office of Technical Services
U. S. Department of Commerce
Washington 25, D.C.

PION-PROTON ELASTIC SCATTERING IN THE ENERGY RANGE 300 TO 700 MeV

Contents

PION-PROTON ELASTIC SCATTERING IN THE ENERGY RANGE 300 TO 700 MeV

Philip M. Ogden

Lawrence Radiation Laboratory
University of California
Berkeley, California

February 20, 1964

ABSTRACT

Differential cross sections for elastic π-p scattering have been measured at eight energies for positive pions and seven energies for negative pions. Energies ranged from 310 to 650 MeV. These measurements were made at the 3-BeV proton synchrotron at Saclay, France. A beam of pions from an internal BeO target was directed into a liquid hydrogen target. Fifty-one scintillation counters and a matrix-coincidence system were used to measure simultaneously elastic events at 21 angles and charged inelastic events at 78 π-p angle pairs. Events were detected by a coincidence of pulses indicating the presence of an incident pion, scattered pion, and recoil proton and the results were stored in the memory of a pulse-height analyzer. Various corrections were applied to the data and a least-squares fit was made to the results at each energy. The form of the fitting function was a power series in the cosine of the center-of-mass angle of the scattered pion. Integration under the fitted curves gave values for the total elastic cross section. The importance of certain angular-momentum states, particularly the D_{13} state near 600 MeV, is discussed. Several possible explanations are given of the enhancement in the π^--p cross sections near 600 MeV.

I. INTRODUCTION

An important, and in many ways basic, interaction for the study and understanding of the forces and phenomena of the subatomic realm is the interaction between the π meson (pion) and the nucleon. In the S-matrix theory of strong interactions, the unitarity of the S matrix results in a coupling among processes. This implies that information about the pion-nucleon interaction is valuable for the description of other interactions. Therefore, it is no surprise that in the 17 years since the discovery of the charged pion in 1947,[1] many experiments have been performed to study this interaction.

As information about the pion-nucleon interaction accumulated, it was seen that the interaction is quite complex. For example, if one looks at the total cross sections for π^+-p and π^--p as functions of the energy of incoming pions, one's attention is immediately drawn to a series of peaks with varying widths and heights.[2]

In this experiment, differential and total elastic cross sections were measured for both positive and negative pions interacting with protons. In Fig. 1 we see plots of the total cross sections for π^+-p and π^--p scattering as functions of the lab kinetic energy of the pion. The vertical lines represent the energies at which the measurements of this experiment were made. The π^+-p interaction was studied at all eight energies, whereas 310 MeV was omitted for π^--p.

A great many experiments have been performed at energies below 310 MeV.[3] This low-energy region, dominated by the $T = 3/2$, $J = 3/2$ (3, 3) resonant state, is quite well understood. Recent extensive measurements at 310 MeV have given a fairly complete description of the pion-nucleon interaction at that energy.[4] On the other hand, considerable information is also available in the energy range from 550 to 1600 MeV.[5]

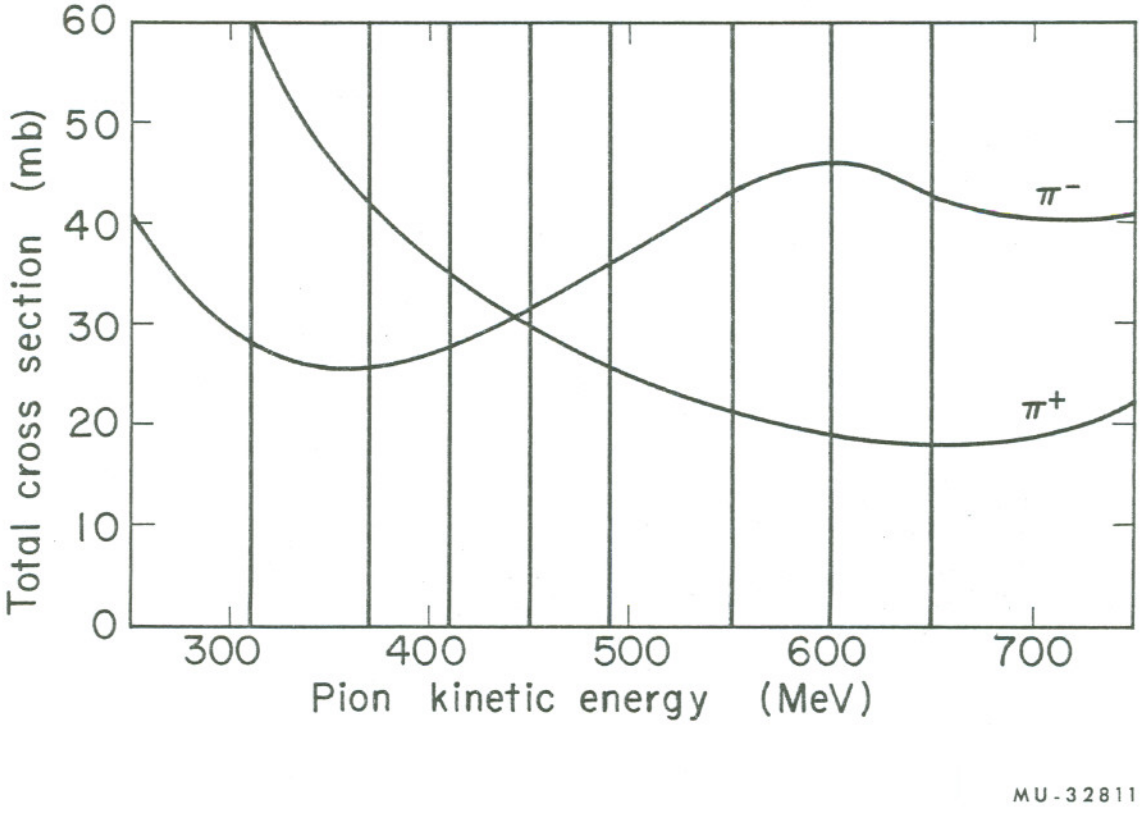

Fig. 1. Total cross sections for $\pi^{\pm}$-p with lines indicating the energies at which the measurements of this experiment were made.

The purpose of our experiment was to obtain information in the 300- to 650-MeV region in an attempt to bridge the gap in the existing data. Several experiments have been done in this region.[6] However, the statistical accuracy of these measurements is in general quite poor and in several cases the gap in energy between measurements is quite large.

In the study of the pion-nucleon interaction, it is of interest to know the role of the various angular-momentum states. Such information can be obtained from a partial-wave analysis, in which the scattering is defined by a set of phase shifts.

As the energy is increased, a partial-wave analysis becomes more and more difficult because more and more angular-momentum states become important. Furthermore, when inelastic processes become important, the phase shifts become complex quantities and this results in a doubling of the number of necessary parameters. For these reasons, a partial-wave analysis at a single energy produces many possible solutions. By requiring that the phase shifts be continuous functions of energy, it is hoped that most solutions can be eliminated.

In order to apply the restrictions of energy continuity, it is necessary to have a closely spaced network of accurate data. Thus, we realize the importance of data in the 300- to 650-MeV range in connecting the low-energy data with the high-energy data.

The experimental procedure and a description of the equipment are presented in Sec. II. In Sec. III one finds the way in which the data were analyzed and the way in which the corrections were applied. The presentation of the results and their interpretation appear in Secs. IV and V, respectively; also presented in Sec. V are the partial-wave equations and a discussion of the importance of the various angular-momentum states.

II. EXPERIMENTAL PROCEDURE AND EQUIPMENT

A. Procedure

The general layout of the experiment is shown in Fig. 2. Positive and negative pions were produced in a BeO target inside Saturne, the Saclay proton synchrotron. By means of a magnetic optical system, a beam of pions with the desired charge was momentum analyzed and focused on a liquid hydrogen target. Four scintillation counters were used to monitor the beam. Because protons in the positive-pion beam had a longer time of flight than pions, response of the counting system to protons was eliminated electronically. Response to electrons and a portion of the muons in the beam was eliminated with a gas Cerenkov counter. Cases in which two beam particles were too close together in time were eliminated electronically.

Scattered pions and their associated recoil protons emerging from the liquid hydrogen target were detected with an array of 46 scintillation counters. Elastic events were detected by a coincidence of pulses indicating the presence of the incident pion, scattered pion, and recoil proton. Geometric restrictions requiring that the event be coplanar or nearly coplanar and at proper pion and proton angles minimized the inelastic contamination. By measuring inelastic events in the region near the elastic events, a correction was determined for the elastic channels. Elastic events at 21 scattering angles and charged inelastic events at 78 π-p off-elastic angle pairs were simultaneously measured and stored in the memory of a pulse-height analyzer. At the end of each run the data in the memory were simultaneously punched on IBM cards and typed by an electric typewriter.

The magnet currents for each beam momentum were determined by the wire-orbit method. The precision of this method was estimated to be about 1%. The beam momentum was also measured by electronically determining the time-of-flight difference between pions and protons in passing between two of the monitor counters. The momentum values from the latter method were within 0.5% of the values obtained

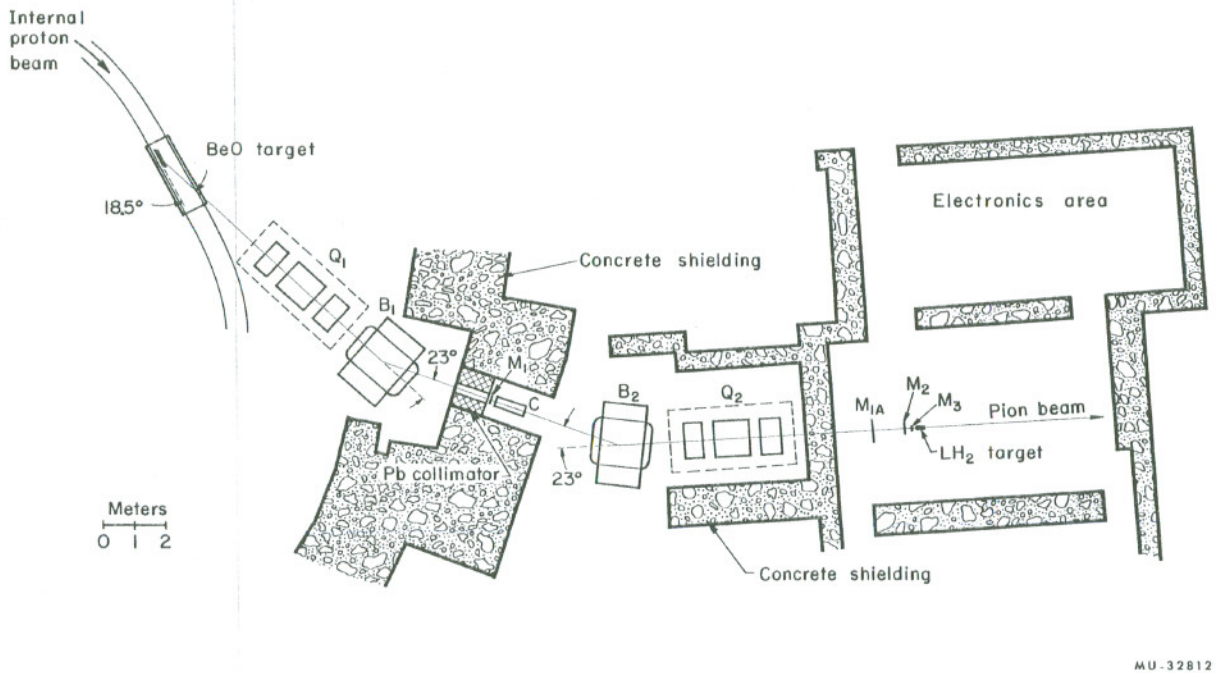

Fig. 2. Plan view of the experimental arrangement. Symbols Q_1, B_1, B_2, and Q_2 represent magnets. The beam counters are labelled M_1, M_{1A}, M_2, M_3, and C. The counters, BeO target, and LH_2 target are not drawn to scale.

by the wire-orbit method.

Empty-target runs were made in order to correct for the contribution to the full-target runs due to interactions in the target walls.

The statistical errors on the differential cross-section data averaged 3 to 3.5%.

B. Equipment

1. Beam Design

The internal Saturne beam of 3-BeV protons was caused to impinge upon a BeO target. The target was an 18.5-deg parallelepiped 10 cm in the direction of the internal proton beam, 1 cm in the horizontal direction perpendicular to the internal beam, and 1.5 cm in the vertical direction. The secondary beam consisted of pions that were created in proton interactions in the BeO target and that emerged from the target at an angle of 18.5 deg relative to the internal beam. As viewed from the direction of the pion beam, the horizontal dimension of the BeO target was 3.2 cm.

The pion beam was produced over a period of approximately 200 msec for each cycle. The accelerator was cycled at the rate of 16.7 times per minute.

A symmetric optical system consisting of two triplet quadrupole magnets (Q_1 and Q_2) and two bending magnets (B_1 and B_2) conducted particles of the proper charge and momentum from the internal target to a position and momentum focus at the hydrogen target. (See Figs. 2 and 3)

A lead collimator (Pb) was incorporated at the intermediate focus to define a spread of $\pm 3\%$ in the beam momentum.

The positive-pion beam also contained protons, positive muons, and positrons and the negative-pion beam also contained negative muons and electrons. Strange particles were present in negligible quantities. The elimination of protons is discussed in Sec. II. B.4. Muon and electron contaminations are discussed in Secs. II. B.3 and III. B.1.

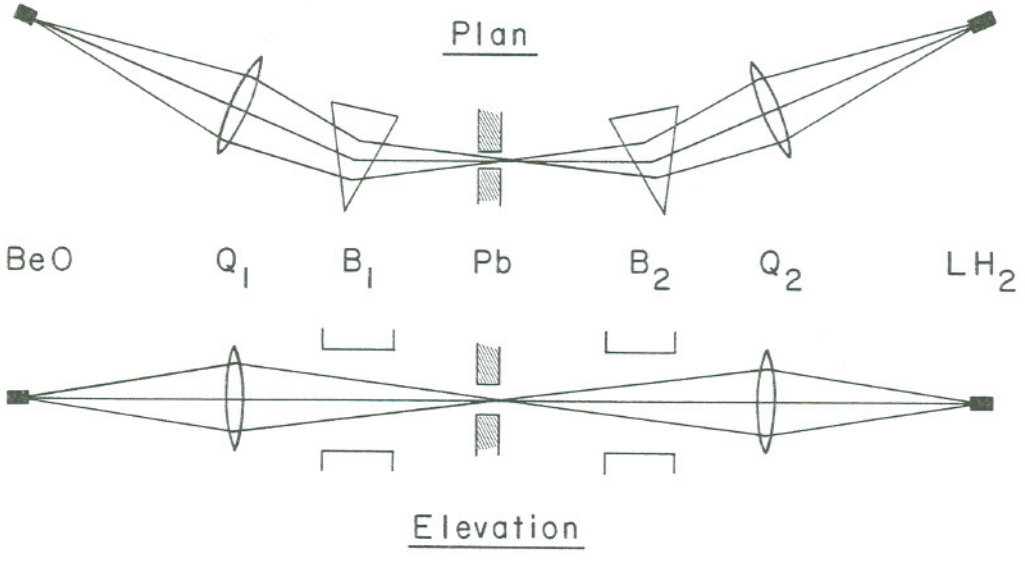

Fig. 3. Schematic representation of the magnetic optical system.

Because of the symmetry of the beam design, the overall magnification was unity. Ideally, one would expect to have a final image at the hydrogen target with the same dimensions as the BeO target—namely, 3.2 cm horizontally and 1.5 cm vertically. However, the actual size of the image was increased by particle scattering and by aberration in the magnetic optical system. In order to minimize the scattering, the beam region was evacuated wherever possible. At the final image the half-maximum dimensions of the beam were 3.5 cm horizontally and 2 cm vertically.

At the hydrogen target the maximum angle of a beam particle relative to the central ray was 1.9 deg.

2. Liquid Hydrogen Target

The hydrogen target was a right circular cylinder with convex rounded ends. The axis of the cylinder lay along the beam line. The target had a length along the axis of 10.3 cm and a radius of 3.2 cm. The radius of curvature of the rounded ends was 6.4 cm. By taking into consideration the variation in length traversed as a function of the position in the beam profile and the angular spread of the beam, the effective length of hydrogen traversed by the beam was determined to be 10.1 cm.

The target flask was made of Mylar 0.1-mm thick. Thin sheets of aluminized Mylar with a total thickness of 0.1mm were placed in the evacuated region surrounding the target. These sheets and the vacuum layer served as a heat shield for the target. The outer window was of Mylar 0.4-mm thick. Holes in the aluminized Mylar at each end and one side of the target flask made accurate positioning possible.

All supports for the target were placed above and below the target or in one quadrant of the horizontal plane. Thus, as viewed down the beam line, the entire right side and the forward 90-deg of the left side were free of material other than the above-mentioned Mylar. The target flask was filled by gravity flow from the reservoir above. Emptying was initiated by closing the boil-off valve, thus increasing the pressure from the evaporating hydrogen and forcing the liquid into the reservoir.

The density of liquid hydrogen[7] under these conditions is 0.0708 g/cm^3. The "empty" target actually contained hydrogen gas of density 0.00136 g/cm^3; the presence of this hydrogen necessitated a 1.9% correction to the effective density of the full target. An additional 0.6% decrease in the effective hydrogen density came from the presence of gas bubbles in the boiling liquid. The latter correction was deduced from the rate of boiling and an estimate of the bubble velocity. It was assumed that the density of bubbles was uniform throughout the region through which the beam passed.

3. Scintillation and Cerenkov Counters

Each scintillation counter used in this experiment consisted of a scintillating plastic detector, a Lucite light pipe, and a magnetically shielded photomultiplier tube with voltage divider base. The scintillation material consisted of a solid solution of terphenyl in polystyrene.

Those counters with high counting rates had high-capacitance, low-resistance voltage divider bases. In the extreme cases, separate high-voltage supplies were used on the last two stages. In this way the drop in gain with high counting rate was kept well within tolerable limits.

All of the scintillation counters used photomultiplier tubes (RCA-6810A), with the exception of the monitor counters, three of which had Amperex tubes (56-AVP) and the other had an RCA-7264 tube.

Four scintillation counters and a Cerenkov counter were used to monitor the beam (see Fig. 2). Counters M_1 and M_3 were beam-defining counters, M_1 being at the intermediate image and M_3 being 15 cm in front of the hydrogen target. The dimensions of M_1 were virtually the same as the aperture of the lead collimator behind which it stood. These dimensions were 6 cm horizontally and 1.8 cm vertically. The thickness of M_1 was 0.8 cm. The M_3 scintillator was a disk with diameter 3.8 cm and thickness 0.3 cm.

Counters M_{1A} and M_2 were large counters designed to detect all of the beam particles. A coincidence of signals from M_1, M_2, and M_3 formed the basis of the beam-monitor system. The signal from

M_{1A} and a second signal from M_2 were used in the double-pulse-rejection system. A discussion of the double-pulse-rejection system is given in Sec. II. B. 4. Counter M_{1A} was 19 cm wide, 13 cm high, and 1 cm thick, and was placed 1.5 m in front of the hydrogen target. Situated 0.5 m in front of the target was M_2, which was 12 cm wide, 6 cm high, and 0.8 cm thick.

In order to improve the uniformity of the signal amplitude from counter M_2, two light pipes and two photomultiplier tubes were used. The two signals were added passively to give a single, more uniform pulse.

In order to reject electronically the electrons and a portion of the muons, a gaseous ethylene Cerenkov counter was placed near the intermediate image. Ethylene was chosen because its index of refraction at pressures easily attainable is in the proper range to distinguish between muons and pions at the energies of this experiment. At 310 MeV, an absolute pressure of 42.5 kg/cm^2 was required.

A description of the Cerenkov counter, C, is given in Ref. 8. Its overall length was 90 cm. A cylindrical mirror with axis along the beam and a plane mirror at 45 deg to the beam served to reflect the light onto the face of a photomultiplier tube (56-AVP).

The signal from the Cerenkov counter was put in anticoincidence with the $M_1M_2M_3$ coincidence. Thus, if a particle were detected by the Cerenkov counter, it was rejected. Curves were made of the fraction of the beam accepted as a function of ethylene pressure in order to determine the optimum pressure for accepting pions and rejecting muons and electrons. Such measurements were made at 370, 500, and 650 MeV. Values for the other energies were determined by interpolation or extrapolation.

Measurements made at the beginning of the experiment with a second, similar Cerenkov counter, placed where the hydrogen target was later placed, were used to determine the number of muons resulting from pion decay after the first Cerenkov counter. This correction is discussed in Sec. III. B.1.

The array of 46 scintillation counters used to detect scattered particles is shown schematically in Fig. 4. Figure 5 is a photograph showing these counters as they were situated around the hydrogen target. The 21 π counters were placed to the right of the beam at various laboratory angles between 25 and 153 degrees. Their purpose was to detect scattered pions.

The solid-angle region available to protons conjugate to the pions detected by the π counters was covered by 25 overlapping counters labelled ρ counters. The ρ counters were combined in 21 groups, each containing from three to seven. Such a group, called a P counter, detected all protons conjugate to the corresponding π counter. The ρ-counter signals for a given group were added electronically. The way in which the counters were combined varied with each energy of the incident-pion beam.

The π counters were 1.3 cm thick. They were designed to subtend 18 deg in ϕ, the azimuthal angle about the beam direction. As the scattering angle increased, the π counters were made wider in order to make the solid angles and intervals approximately uniform in the center-of-mass system. Table I gives the laboratory central angle and solid angle along with the width of each π counter. The solid angles, and the cosines of the scattering angles, both in the center-of-mass system, are given for each energy in Table II.

The ρ counters were 1 cm thick and 10.5 cm wide. They were rectangular in shape except near the beam where they were trapezoidal. Their lengths were such as to subtend approximately 22 deg in ϕ.

An additional scintillation counter, S_0, was placed near the hydrogen target, as shown in Fig. 4. Its purpose is discussed in Sec. II. B.4. This counter, which was 1 cm thick, was designed so that a straight line from any point in the target to any point on any π counter would pass through S_0.

4. Electronics

Block diagrams of the monitor-system electronics and the coincidence-matrix electronics are given in Figs. 6 and 7 respectively. The symbols used in these two figures are defined in Table III. The photograph in Fig. 8 shows a portion of the electronic equipment.

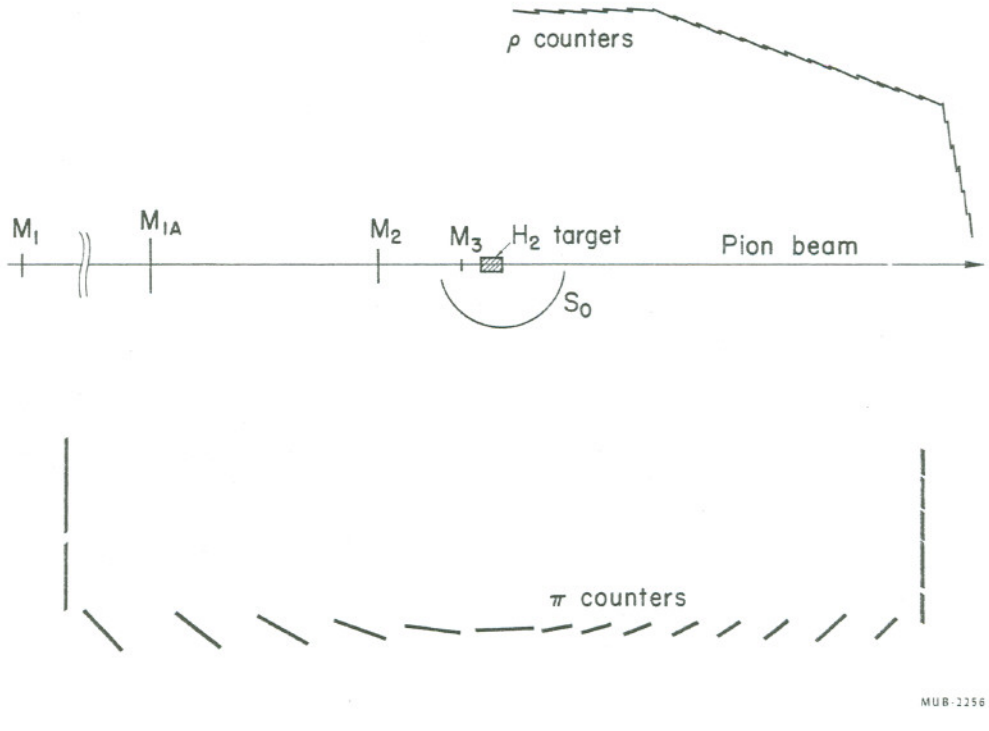

Fig. 4. Plan view of scintillation-counter array.

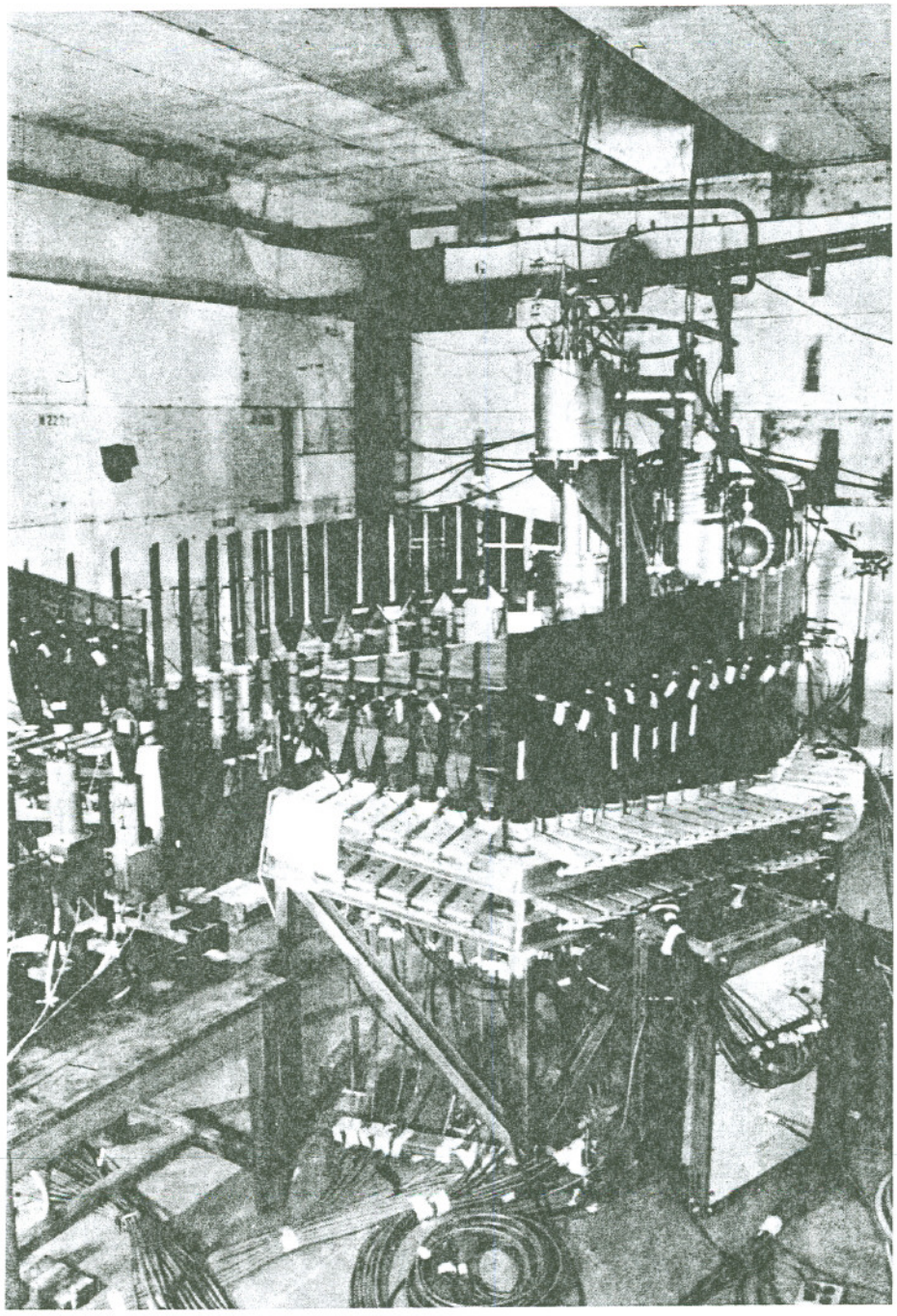

ZN-4081

Fig. 5. Scintillation counters as they were situated around the hydrogen target.

Table I. Pion-counter data, laboratory system.

Counter Number	Counter width (cm)	Central angle (deg)	Solid angle (msr)
1	10.8	25.0	6.251
2	13.2	28.2	8.023
3	12.2	31.4	7.701
4	20.7	35.1	13.232
5	13.5	38.8	8.587
6	12.7	42.7	11.377
7	17.8	47.1	18.348
8	12.7	52.0	15.306
9	12.7	57.0	17.654
10	12.7	62.0	19.468
11	12.7	68.0	21.369
12	12.7	74.0	22.499
13	12.7	80.0	24.044
14	25.4	88.0	49.059
15	25.4	99.0	48.605
16	25.4	110.0	43.983
17	25.4	120.0	36.847
18	25.4	129.0	30.427
19	25.4	137.0	23.013
20	30.2	144.0	19.315
21	41.7	153.0	24.836

Table II(a). Cosines of pion scattering angles (θ^*), c.m. system.

Counter number	Incident-pion laboratory kinetic energy (MeV)							
	310	370	410	450	490	550	600	650
1	0.823	0.812	0.805	0.798	0.792	0.782	0.773	0.765
2	0.778	0.765	0.757	0.748	0.740	0.728	0.718	0.708
3	0.729	0.714	0.705	0.695	0.685	0.671	0.659	0.648
4	0.669	0.651	0.639	0.628	0.617	0.600	0.586	0.573
5	0.604	0.584	0.571	0.558	0.545	0.526	0.511	0.496
6	0.533	0.510	0.495	0.480	0.466	0.445	0.428	0.412
7	0.450	0.425	0.408	0.392	0.376	0.354	0.335	0.317
8	0.355	0.328	0.310	0.292	0.276	0.251	0.231	0.212
9	0.258	0.228	0.209	0.191	0.173	0.148	0.127	0.107
10	0.160	0.130	0.110	0.091	0.073	0.047	0.026	0.006
11	0.045	0.014	-0.006	-0.025	-0.043	-0.070	-0.090	-0.110
12	-0.067	-0.098	-0.118	-0.136	-0.154	-0.180	-0.200	-0.219
13	-0.174	-0.204	-0.223	-0.241	-0.258	-0.283	-0.302	-0.320
14	-0.308	-0.336	-0.353	-0.370	-0.386	-0.408	-0.425	-0.441
15	-0.472	-0.496	-0.511	-0.525	-0.538	-0.556	-0.570	-0.584
16	-0.613	-0.632	-0.644	-0.655	-0.665	-0.679	-0.691	-0.701
17	-0.720	-0.735	-0.744	-0.752	-0.760	-0.771	-0.779	-0.787
18	-0.800	-0.811	-0.818	-0.824	-0.830	-0.838	-0.844	-0.850
19	-0.860	-0.868	-0.873	-0.877	-0.881	-0.887	-0.891	-0.895
20	-0.903	-0.908	-0.912	-0.915	-0.918	-0.922	-0.925	-0.928
21	-0.946	-0.949	-0.951	-0.953	-0.954	-0.957	-0.958	-0.960

Table II(b). Pion solid angles (msr), c. m. system.

Counter number	Incident-pion laboratory kinetic energy (MeV)							
	310	370	410	450	490	550	600	650
1	11.361	11.957	12.347	12.730	13.107	13.662	14.114	14.557
2	14.258	14.964	15.422	15.871	16.311	16.954	17.476	17.984
3	13.355	13.972	14.317	14.759	15.138	15.689	16.132	16.562
4	22.237	23.175	23.775	24.356	24.920	25.731	26.379	27.001
5	13.951	14.480	14.815	15.137	15.447	15.889	16.238	16.570
6	17.787	18.377	18.746	19.098	19.433	19.905	20.273	20.618
7	27.410	28.170	28.639	29.080	29.493	30.066	30.503	30.905
8	21.672	22.140	22.422	22.680	22.918	23.238	23.474	23.684
9	23.608	23.969	24.178	24.363	24.527	24.735	24.878	24.995
10	24.540	24.763	24.881	24.977	25.052	25.131	25.169	25.185
11	25.047	25.093	25.097	25.082	25.050	24.976	24.892	24.792
12	24.490	24.364	24.260	24.143	24.014	23.804	23.615	23.417
13	24.300	24.014	23.811	23.601	23.386	23.055	22.774	22.491
14	44.964	44.068	43.470	42.874	42.284	41.409	40.693	39.990
15	39.159	37.991	37.241	36.513	35.808	34.791	33.980	33.200
16	31.425	30.224	29.470	28.749	28.061	27.085	26.319	25.593
17	23.854	22.793	22.134	21.512	20.923	20.095	19.454	18.851
18	18.215	17.319	16.768	16.251	15.765	15.087	14.565	14.077
19	12.965	12.283	11.867	11.477	11.113	10.607	10.219	9.859
20	10.397	9.824	9.476	9.152	8.849	8.430	8.110	7.814
21	12.753	12.019	11.575	11.162	10.778	10.249	9.846	9.473

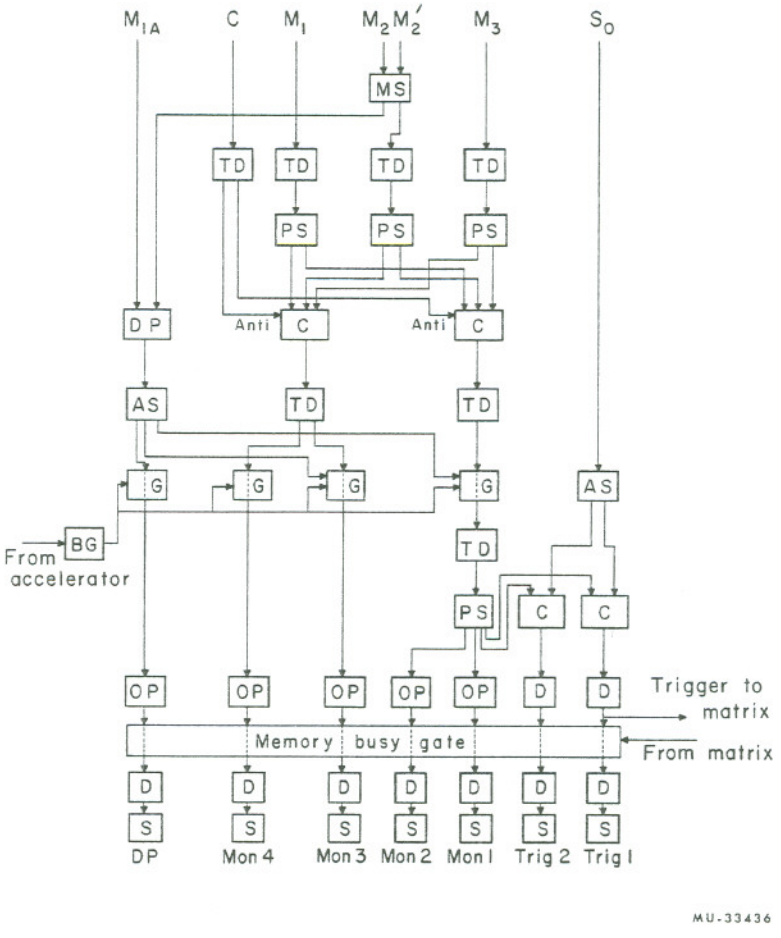

Fig. 6. Block diagram of the monitor electronics system.

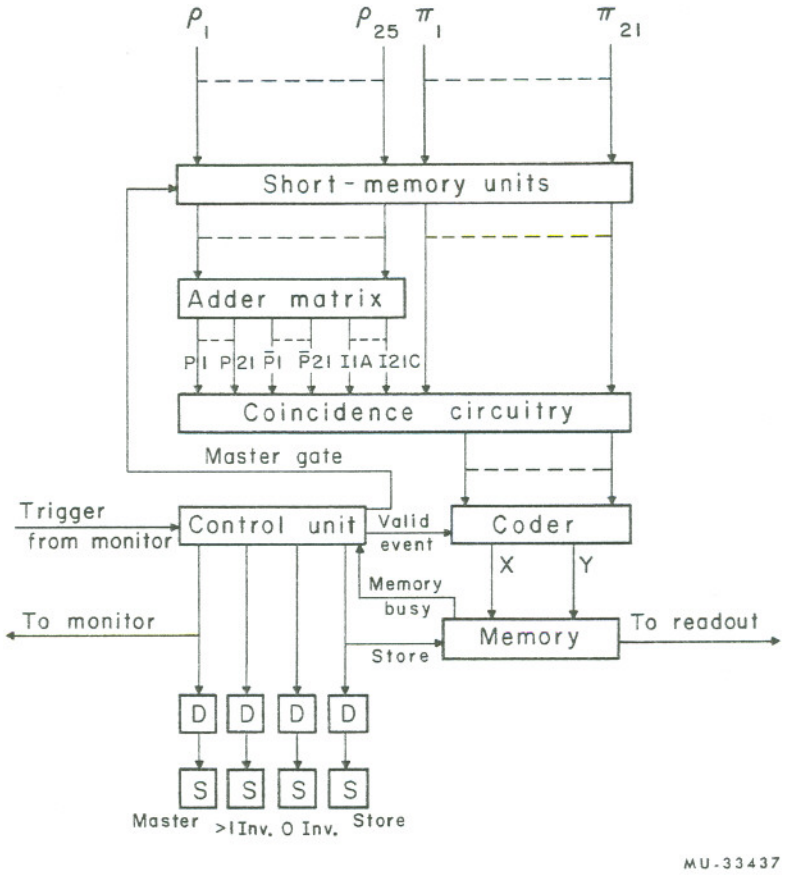

Fig. 7. Block diagram of the coincidence-matrix electronics system.

Table III. Key to symbols used in Figs. 6 and 7.

Symbol	Description
AS	Active splitter
BG	Beam-gate generator
C	Coincidence circuit
D	10-Mc discriminator
DP	Double-pulse-rejection system
G	Gate circuit
MS	Passive mixer-splitter
OP	20-Mc octal prescaler
PS	Passive splitter
S	5-Mc scaler
TD	20-Mc tunnel-diode discriminator

Detailed descriptions of many of the circuits used in this experiment are given in the LRL Counting Handbook.[9] Other circuits are described in Refs. 10, 11, and 12.

The three main purposes of the monitor system were: (a) to determine which beam particles were acceptable, (b) to count the accepted particles, and (c) to trigger the coincidence matrix whenever there was a possibility of an acceptable scattering event accompanying an accepted beam particle.

The basic sequence of the monitor logic can be followed by looking at the elements in the vertical line below M_3 in Fig. 6. A coincidence $M_1M_2M_3\overline{C}$ was formed. (The bar over the C indicates anticoincidence.) The resultant signal was either passed or blocked by a special gate circuit, triggered by the double-pulse-rejection system. Those signals passed by the gate were then scaled. The same signal that was scaled was also put into a coincidence with S_0 and the resultant coincidence $M_1M_2M_3\overline{C}S_0$ was used as the trigger for the matrix system. By requiring a coincidence with S_0, the repetition rate of the trigger was greatly reduced without loss of acceptable scattering events, since any particle from the target passing through one of the π counters must also pass through the S_0 counter.

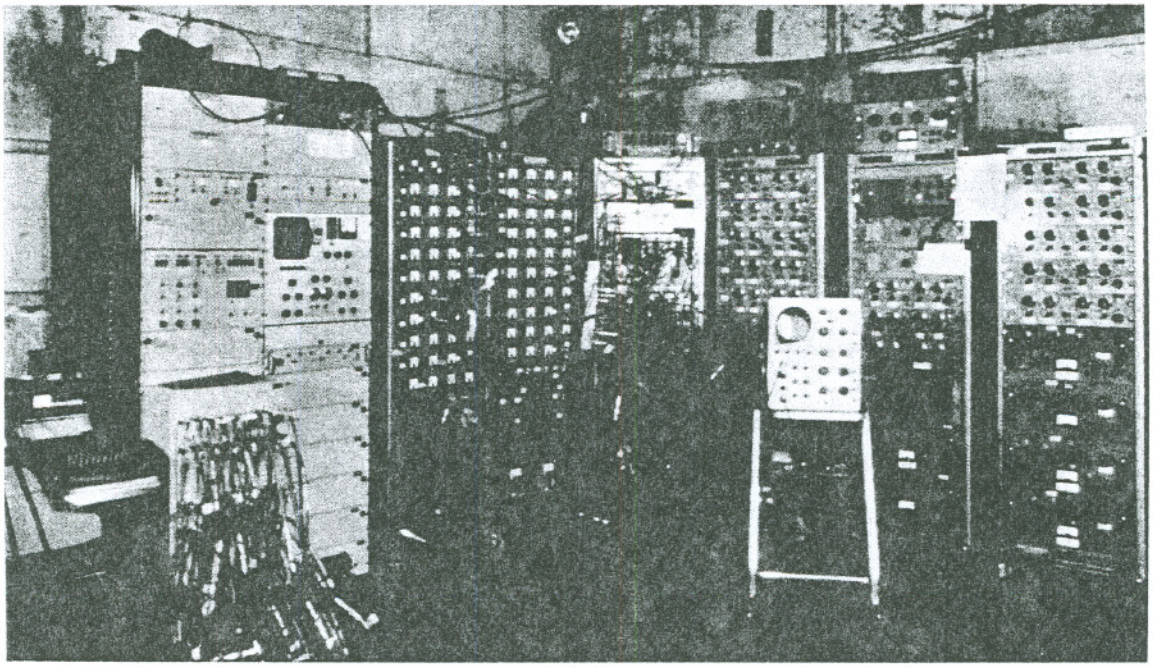

ZN-4082

Fig. 8. The portion of the electronics in the counting area.

The remaining elements of Fig. 6 served to check the performance and reliability of the basic sequence as well as to provide additional interesting but nonessential information, such as the fraction of the beam rejected by the double-pulse-rejection system.

As mentioned previously, protons were present in the positive-pion beam. However, in passing from counter M_1 to counter M_3, a proton took 24 nsec longer than did a pion at 650 MeV. This time difference was even greater at lower energies. The resolving time of the monitor coincidence circuit was 10 nsec so that protons were rejected very effectively.

The double-pulse-rejection system was designed to reject those beam particles accompanied within about 60 nsec by a second particle. In this way three types of undesirable events were eliminated.

The first type is one in which two pions were so close together in time that they could not be resolved by the monitor electronics. The monitor system was limited to a 20-Mc repetition rate, which meant that two particles less than 50 nsec apart appeared as one. Therefore, although two particles entered the target with a probability of scattering, only one was counted by the monitor. Such occurrences would lead to an error in the normalization of the differential cross section.

The second type is similar to the first. However, in this type, of the two particles that arrived at the target close together in time, only one was a pion that passed through M_1, M_2, and M_3. The other could have been a pion that missed M_1 or M_3, or possibly both, or it could have been a proton. Although such particles would not normally be accepted, they could cause erroneous results when accompanied by a desirable beam particle. As in the first case there is double probability of scatter but only one monitor count.

The third type is one in which an accidental monitor coincidence was generated. Consider a pion that passed through M_1, M_{1A}, and M_2 but not M_3, and was closely associated with another particle (not necessarily a pion), which passed through M_3. Since M_{1A} and M_2 were large counters, essentially all particles that passed through M_3 also

passed through M_{1A} and M_2. Thus, although neither particle was an acceptable particle, together they generated a monitor coincidence. However, since they both passed through M_{1A} and M_2, the counters that triggered the double-pulse-rejection system, this type of event was eliminated.

The circuits of the double-pulse-rejection system are described fully in Ref. 11. The photomultiplier signal was split, the resulting signals delayed, and then these signals recombined to give one wide pulse. For two input pulses close together in time, the resultant overlapping wide pulses formed a double-amplitude pulse easily distinguished by a discriminator. When such an event occurred for both M_{1A} and M_2, the wide gating signal generated closed the gate in the monitor logic sequence.

The heart of the experimental apparatus lay in the coincidence-matrix system depicted in Fig. 7. It was there that the scattering events were detected and recorded.

Signals from the π and ρ counters were fed into tunnel-diode pulse shapers. The shaped pulses were then passed to the short-memory units where a coincidence was formed with the trigger from the monitor system. The resolving time of this coincidence was of the order of 40 nsec. However, the output signal, several μsec long, from the short-memory units permitted use of slow-pulse techniques in the succeeding circuitry. In this way the reliability of the system was considerably improved. Obviously, such slow-pulse techniques imposed a dead time on the system. For this reason, a gating signal was generated to gate off the scalers in the monitor system until the matrix system was ready for a new event.

The ρ signals from the short-memory units were added in the adder matrix to form the P signals corresponding to the P counters mentioned in Sec. II. B.3. In this part of the system the ρ signals were also routed to the various inelastic channels. Plug-in circuit boards were used in the adder matrix in order to permit changing the array for each beam energy.

Signals from the adder matrix as well as the π signals from the short-memory units were passed to the coincidence matrix. There the 99 possible coincidence combinations corresponding to the 21 elastic and 78 inelastic channels were detected. Outputs from the coincidence matrix passed to the coder, which determined the memory address in which the event was to be stored.

In the control unit a check was made of the number of coincidences occurring in the matrix. If for a given trigger, no coincidence resulted, a signal was sent to the Zero-Invalid (0 Inv) scaler. Events involving two or more coincidences were recorded in the Greater than One-Invalid (> 1 Inv) scaler and were not stored. This occurred very seldom, and it was estimated that the number of desirable events lost in this manner was negligible. When one and only one coincidence occurred, a signal from the control unit allowed the memory to store the event.

At the end of each run, the data in the memory were recorded by an electric typewriter and also punched on IBM cards.

Two test systems were used in setting up and periodically checking the entire electronics complex. Both systems simulated π-ρ coincidences in a cyclical, systematic manner.

In the light-pulse system, pulsed argon lamps were used on each of the π and ρ counters as well as on M_2, M_3, and S_0.[13]

With the electrical-pulse system, the counters were bypassed and electrical pulses were fed directly to the tunnel-diode shapers and the control unit.

III. DATA ANALYSIS

A. General Analysis

The definition of the differential cross section $d\sigma(\theta^*)/d\Omega^*$ yields the following expression for the number of particles scattered at the c.m. scattering angle, θ^*, into the c.m. solid angle, $d\Omega^*$:

$$\frac{dN(\theta^*)}{d\Omega^*} = N_0 \left[1 - \exp\left(-nx \frac{d\sigma(\theta^*)}{d\Omega^*}\right)\right]. \tag{1}$$

Here, N_0 is the number of particles incident on the target, n is the number of protons per unit volume of the target, and x is the target length.

Since the exponential argument is small compared to one, the exponential term can be replaced by one minus the argument. This leaves

$$\frac{dN(\theta^*)}{d\Omega^*} = N_0 \, nx \, \frac{d\sigma(\theta^*)}{d\Omega^*}. \tag{2}$$

We now assume that

$$\frac{dN(\theta^*)}{d\Omega^*} = \frac{\Delta N(\theta^*)}{\Delta\Omega^*}. \tag{3}$$

For the ith channel we define

$$R_i = \frac{\Delta N(\theta_i^*)}{N_0}, \tag{4}$$

and replace $\Delta\Omega_i^*$ by Ω_i^*. With these changes, Eq. (2) becomes

$$\frac{d\sigma(\theta_i^*)}{d\Omega_i^*} = \frac{R_i}{nx\Omega_i^*}. \tag{5}$$

The quantity R_i is the ratio of the coincidence counts in the ith channel to the number of monitor counts. In terms of coincidences we can write

$$R_i = \frac{M_1 M_2 M_3 \bar{C} S_0 \pi_i P_i}{M_1 M_2 M_3 \bar{C}} . \qquad (6)$$

For convenience, we write Eq. (6) in a shorter form:

$$R_i = \frac{\pi_i}{M} . \qquad (7)$$

The statistical error can be written as

$$\Delta R_i = \frac{(\pi_i + 1)^{1/2}}{M} . \qquad (8)$$

An additional term in Eq. (8), involving the statistical error ΔM in the number of monitor counts M, is much smaller than the term shown and has been neglected.

Ideally, the R_i and ΔR_i of Eqs. (7) and (8) could be put into Eq. (5) to give the differential cross section and its error. However, four modifications must be made on the ideal relationship.

The first modification stems from the fact that the experiment was not run continuously, but was divided into many separate runs. Thus, we must sum over the various runs to obtain average rates.

$$\bar{R}_i = \frac{\sum_{j=1}^{n} \pi_{ij}}{\sum_{j=1}^{n} M_j} , \qquad (9)$$

and

$$\Delta \bar{R}_i = \frac{\left(1 + \sum_{j=1}^{n} \pi_{ij}\right)^{1/2}}{\sum_{j=1}^{n} M_j} , \qquad (10)$$

in which j is the run number and n is the number of runs.

The circumstance that scattering occurs in material around the hydrogen target suggests a second change in the analysis. In addition to the full target runs, empty target runs were made and the subtracted

rates give the true rate from hydrogen alone.

$$\bar{R}_i = \bar{R}_{i(\text{full})} - \bar{R}_{i(\text{empty})} \tag{11}$$

$$\Delta\bar{R}_i = \left[(\Delta\bar{R}_{i(\text{full})})^2 + (\Delta\bar{R}_{i(\text{empty})})^2 \right]^{1/2} \tag{12}$$

A third modification comes from an infrequent, but nevertheless sometimes present, inconsistency of the data. We first consider the kth run alone:

$$R_{ik} = \frac{\pi_{ik}}{M_k} ; \tag{13}$$

$$\Delta R_{ik} = \frac{(\pi_{ik} + 1)^{1/2}}{M_k} . \tag{14}$$

Next, an average is made over all the runs except the kth run:

$$\bar{R}_{ik} = \frac{\sum_{j \neq k} \pi_{ij}}{\sum_{j \neq k} M_j} ; \tag{15}$$

$$\Delta\bar{R}_{ik} = \left[\frac{\sum_{j \neq k} M_j (R_{ij} - \bar{R}_{ij})^2}{(n-2) \sum_{j \neq k} M_j} \right]^{1/2} . \tag{16}$$

The error $\Delta\bar{R}_{ik}$ is not a statistical error, but a measure of the reproducibility of all the runs except the kth run.

The data for the ith channel of the kth run were rejected if

$$| R_{ik} - \bar{R}_{ik} | > 3(\Delta R_{ik} + \Delta\bar{R}_{ik}). \tag{17}$$

Less than 0.2% of the data was rejected on this basis.

The fourth modification to the ideal relationship is the application of corrections to the data. These corrections and their associated errors are discussed in Sec. III. B.

B. Corrections to Data

1. Beam Contamination

The presence of particles other than pions in the beam was discussed in Sec. II. B.1. Protons were eliminated by time of flight. Electrons and some muons were eliminated by the Cerenkov counter, C. Calculation indicated that the number of K mesons was negligible. The remaining contamination consisted of muons arising from the decay of pions after the Cerenkov counter.

Since muons have a very small cross section for nuclear scattering, one can correct for their presence in the beam simply by subtracting the number of them from the monitor.

Both measurement and calculation were used in determining the correction. An ethylene Cerenkov counter C_2, similar to the Cerenkov counter C, was placed at the hydrogen-target position. A 10-cm diameter scintillation counter M_4 was placed behind C_2. Coincidences $M_1M_2M_3\bar{C}C_2M_4$ and $M_1M_2M_3\bar{C}M_4$ were measured for a range of ethylene pressures. The ratio of these two quantities indicated the fraction of the beam particles with velocities above the threshold of the Cerenkov counter for the pressure under consideration. A typical curve of this ratio as a function of pressure is shown in Fig. 9.

Muons resulting from pion decay after the last bending magnet B_2 had a spectrum of momenta. They were detected gradually as the pressure was increased and thus produced a sloping contribution to the pressure curve. The magnitude of this spectral contribution was calculated for each pressure from the pion lifetime, kinematics of pion decay, and beam geometry.

A second sloping contribution to the pressure curve came from delta rays. As the beam particles passed through the Cerenkov counter, delta rays were formed. Occasionally one of these delta rays had sufficient energy to be detected by the Cerenkov counter. The number of delta rays was directly proportional to the density of the ethylene. Since the pressure and density were linearly related, the delta rays gave a linear contribution to the pressure curve. The magnitude of this contribution for all pressures was determined by observing the slope of the

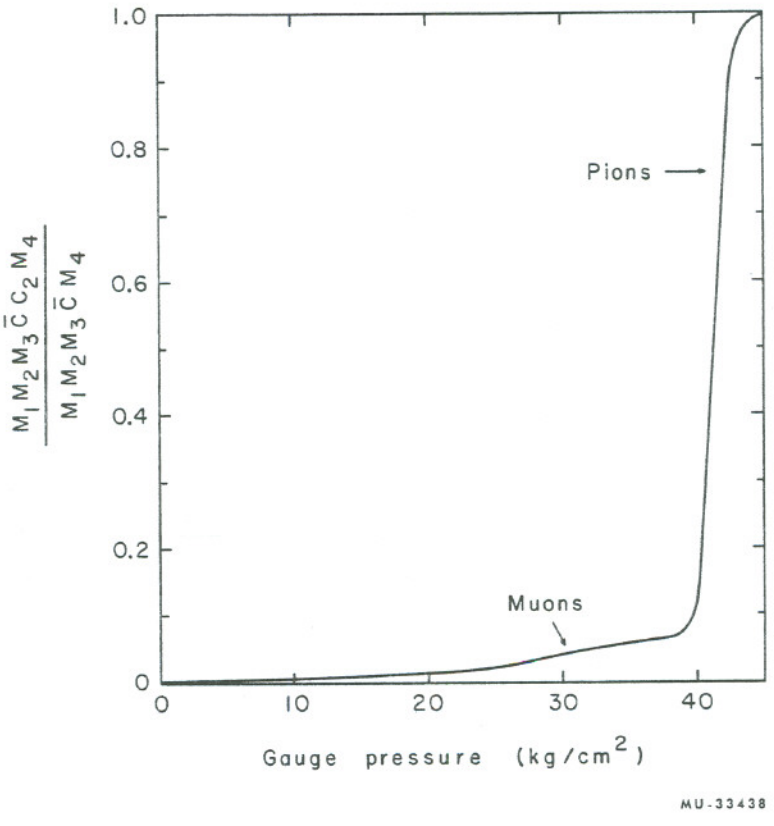

Fig. 9. Cerenkov pressure curve for 370-MeV π^-.

pressure curve at pressures below the muon threshold.

Muons resulting from pion decay before B_2 were momentum analyzed by B_2. Therefore, muons in this category that also passed through M_3 had the same momentum as the pions. All such particles were detected at and above a certain threshold pressure in the Cerenkov counter and thus gave rise to a flat plateau in the pressure curve.

By subtracting the spectral muon contribution and the delta-ray contribution from the measured values of the pressure curve, it was possible to determine the magnitude of the monoenergetic contribution. The sum of the monoenergetic contribution and the total spectral contribution constituted the correction applied to the monitor. A plot of the muon contamination as a function of pion-beam energy is shown in Fig. 10. The total correction ranged from 2.25% at 650 MeV to 4.1% at 310 MeV and was the same for positive- and negative-pion beams.

2. Inelastic Scattering

Although the geometric restrictions of the elastic channels eliminated much of the inelastic contamination, a small portion of inelastic scattering was detected. In order to correct for the presence of such undesirable events, coincidences were measured between the π counter of a given channel and various ρ counters on either side of the corresponding P counter. In this way, at each energy the inelastic background at 78 π-p angle pairs was measured. These 78 combinations for the 370-MeV case are identified with the letter I in Table IV.

The inelastic rates were put on a comparable basis by dividing each by its respective solid-angle factor. The normalized inelastic rates can be thought of as points on a surface

$$z = f(x, y), \tag{18}$$

where x and y are the π and p angles. By means of the method of least-squares, a surface was fitted to the 78 data points. Interpolation to the angles of the elastic channels was then done by reading the values from the fitted surface. Each of these values was then multiplied by the respective solid-angle factor to give the inelastic correction for each elastic channel. An error on the correction was determined from the error matrix of the least-squares fit. This error was combined with the statistical error in the usual right-triangle manner for uncorrelated errors.

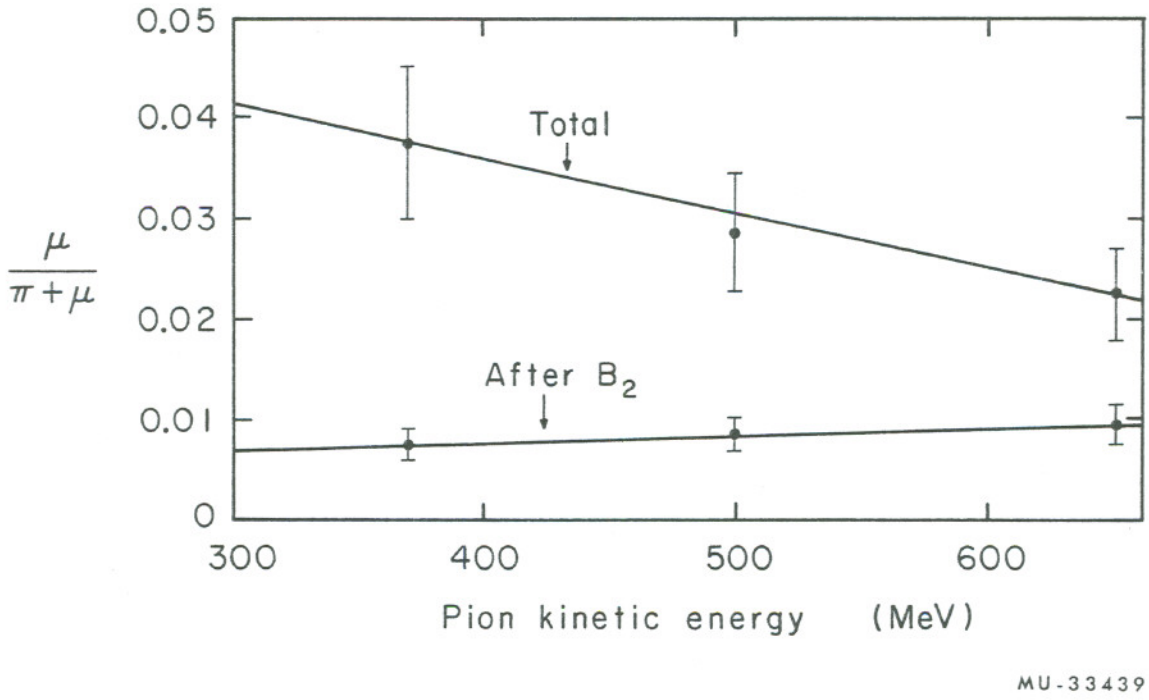

Fig. 10. Muon contamination as a function of pion energy.

Table IV. Scattering possibilities for each π-ρ combination at 370 MeV.

ρ \ π	1	2	3	4	5	6	7	8	9	10	11	12	13	14	15	16	17	18	19	20	21
1	I	I	R	R	R	R															
2	F	F	I	R	R	R															
3	F	F	F	X	R	R	R	I													
4	F	F	F	F	X	R	R	I	I												
5	I	F	F	F	F	X	X	R	I	I	I										
6	I	I	F	F	F	X	X	X	I	I	I										
7		I	I	I	F	F	X	X	X	I	I	I									
8			I	I	I	F	X	X	X	F	F	I	I								
9				I	I	I	F	X	X	X	F	F	I	I							
10					I	I	I	R	X	X	F	F	F	I							
11						I	I	I	R	X	F	F	F	F	I						
12							I	I	R	R	X	F	F	F	I	I					
13									I	R	R	F	F	F	F	I	I				
14										R	R	I	F	F	F	I	I				
15										R	R	R	I	F	F	F	I				
16											R	R	I	F	F	F	F	I			
17											R	R	I	I	F	F	F	I			
18											R	R		I	F	F	F	F	I		
19												R	R	I	I	F	F	F	I	I	I
20												R	R		I	F	F	F	F	I	I
21												R	R		I	I	F	F	F	F	I
22												R	R	R		I	I	F	F	F	F
23													R	R			I	I	F	F	F
24													R	R				I	I	F	F
25														R				I	I	I	F

F - Forward elastic
R - Reverse elastic
X - Forward and reverse elastic
I - Inelastic
Blank - Inelastic (not used)
Boxes represent elastic channels.

The magnitude of the average inelastic background for 600-MeV π^- is indicated by a dashed line in Fig. 11. The data points in Fig. 11 have been corrected for the inelastic background.

3. Reverse Elastic Scattering

For the elastic channels in which both the π counter and the P counter were near 45 deg in the lab, elastic events were detected in which the pion passed through the P counter and the proton through the π counter. Such events are called reverse elastic events. They were present in addition to the normal forward elastic events. The resolution time of the short-memory coincidences was of the order of 40 nsec, whereas the separation between forward elastic pions and reverse elastic protons or between forward elastic protons and reverse elastic pions was 10 nsec or less. Thus, we see that the electronics accepted both the forward and the reverse elastic events. In order to reduce the data to that from forward scattering alone, a reverse elastic correction was calculated.

In Table IV, the π-ρ combinations at 370 MeV with forward scattering only are labelled F, and the combinations with reverse only are labelled R. Those combinations for which the two regions overlap are labelled X. The elastic channels are indicated in Table IV by boxes. Those boxes in which there is at least one X represent elastic channels for which a reverse elastic correction was needed.

The reverse c.m. solid angle Ω_R^* was calculated for each channel by means of an IBM computer. The calculation consisted of a weighted average taking into consideration

a. the beam-momentum profile
b. the horizontal beam-intensity profile
c. the angular convergence of the beam
d. the position of the scatter in the target.

The same computer program also calculated the average c.m. angle θ_R^* for reverse scattering.

The experimental rate R_{exp} at a c.m. angle θ_F^* can be expressed in a manner analogous to Eq. (5) of Sec. III. A.

$$\frac{R_{exp}}{nx} = \Omega_F^* \frac{d\sigma(\theta_F^*)}{d\Omega^*} + \Omega_R^* \frac{d\sigma(\theta_R^*)}{d\Omega^*} . \qquad (19)$$

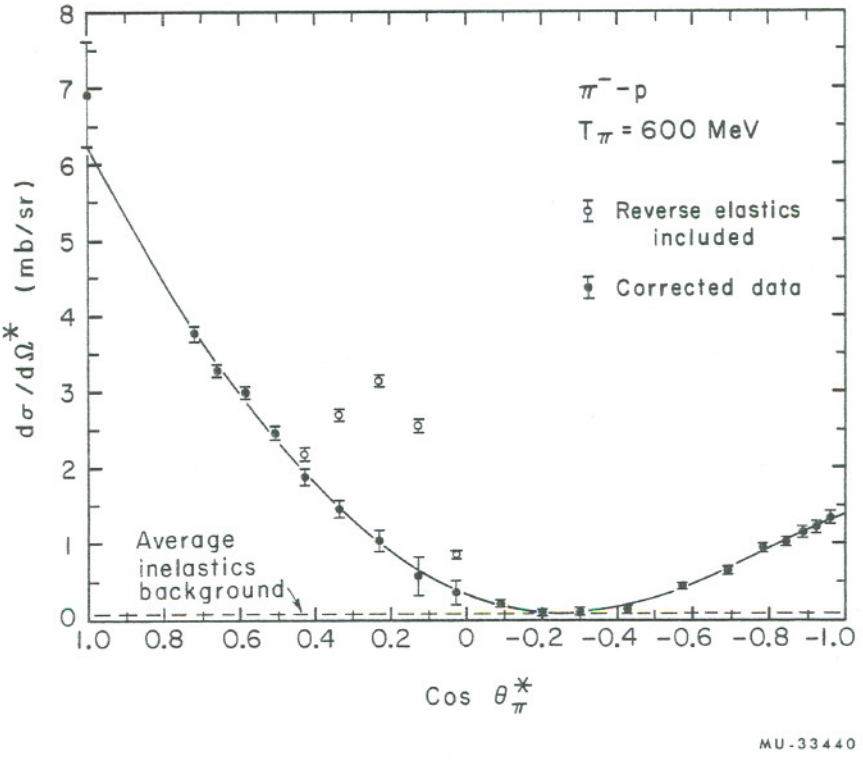

Fig. 11. Data for 600-MeV π^- both with and without the reverse elastic correction. The average-inelastic background is also shown.

Here, Ω_F^* is the c.m. solid angle for forward scattering. We now solve for the desired cross section.

$$\frac{d\sigma(\theta_F^*)}{d\Omega^*} = \frac{R_{exp}}{nx\Omega_F^*} \frac{d\sigma(\theta_R^*)\Omega_R^*}{d\Omega^* \Omega_F^*} . \qquad (20)$$

The cross section at the reverse angle was obtained from the measurements in the other channels. However, several of the other channels also required a reverse elastic correction. The problem was solved by an iterative procedure in which a least-squares fit was made to the data. This fit was used to calculate reverse corrections, and these corrections were applied to the data. A new fit was then made and the process was continued until it converged, i.e., until an additional cycle had a negligible effect on the data.

From Eq. (20) we can see that the error in the corrected cross section has contributions from the errors in the reverse solid angle and reverse cross section in addition to the statistical error ΔR_{exp}. The error in the reverse cross section was determined from the error matrix of the least-squares fit. The error in the reverse solid angle was estimated by considering the effect of a 1% change in beam momentum and a 2-mm displacement of the hydrogen target.

In Fig. 11, the data for 600-MeV π^- are plotted both with and without the reverse elastic correction.

4. Secondary Scattering

There was a finite probability that a scattered particle would rescatter in the hydrogen, the target walls, or the S_0 counter. As a result, some valid elastic events were lost.

By means of a computer program, and with the aid of information from other experiments on π-N and N-N scattering, a correction for the secondary scattering loss was calculated. This correction was calculated for both the forward and the reverse elastic events.

The magnitude of the correction was a few percent except when the pion energy was in the neighborhood of the energy of the (3,3) resonance, i.e., near 200 MeV. In this case, the correction rose as high as 8%.

5. Low-Energy Protons

As the pion angle was decreased and the corresponding proton angle increased, a point was reached where the protons did not have sufficient energy to escape from the target. For each beam energy it was necessary to determine which channels were unreliable due to stopping protons. The data from such channels were not used. At 310 MeV, the lowest beam energy, it was necessary to eliminate the first five channels. As the beam energy was increased, more channels became reliable.

In addition to the problem of stopping protons in the forward elastic case, there were two channels at 310 MeV and one at 370 MeV for which a portion of the reverse protons could not escape from the target.

In order to determine the fraction of reverse protons that stopped before reaching the π counter, a computer program was used to make range calculations for a network of angles and target points. A weighted average was made, taking into consideration:

a. the beam-momentum profile
b. the horizontal and vertical beam-intensity profiles
c. the angular convergence of the beam
d. the shape of the hydrogen target.

The correction due to stopping reverse protons and the error associated with this correction were applied to the calculated reverse solid angle before the reverse elastics correction was applied.

6. Miscellaneous Corrections

An additional correction to the data arose from the finite width of the counters. If the differential cross section had a nonzero second derivative, the average cross section across the angular width of the counter was not the same as the value of the cross section at the central angle. By integrating the fitted curve across the counter, the average cross section was calculated and compared with the measured value to give the correction. Since the correction to the data was taken from the data points themselves, an iteration procedure was followed.

The magnitude of the change in the data points from this correction was always very small.

In order to keep the proper normalization, it was necessary to correct the beam-monitor counting rate for those particles scattered before the center of the hydrogen. This gave the intensity of incident pions at the scattering center. This correction depended slightly on the charge and energy of the beam, but was of the order of 1%.

Several runs were made with the signals of some of the π or ρ counters delayed in order to measure the number of accidental coincidences. Such events were found to be present in negligible quantities.

The presence of accidentals in the beam-monitor system was discussed in Sec. II. B.4. The double-pulse-rejection system eliminated all but a negligible number of such events.

The final corrected data with the total errors are presented in Sec. IV.

IV. RESULTS

A. Differential Cross Sections

The results of the differential-cross-section measurements and the associated errors in standard deviations are shown in Tables V through XII. As mentioned in Sec. III. B.5, some of the small-angle data have been omitted because of the low energy of the recoil proton.

The values given for $\cos\theta^* = 1.0$ are theoretical values obtained from the optical theorem and dispersion relations. The dispersion-relations calculation is that of Cence, Cheng, and Chiu.[14]

B. Least-Squares Fitted Curves

By the method of least-squares, a curve of the form

$$\frac{d\sigma(\theta^*)}{d\Omega^*} = \sum_{n=0}^{N} a_n \cos^n \theta^* \qquad (21)$$

was fitted to the data.[15] The coefficients a_n were determined by the least-squares calculation. The error matrix of the least-squares fit was used to determine the errors in the coefficients.

The differential-cross-section data and fitted curves are plotted in Figs. 12 through 26. The dispersion-relations points were used in making the fits. For π^+-p, a fourth-order fit—i.e., N = 4—was used at all energies. In the case of π^--p, a fourth-order fit was used at 370 and 410 MeV, and a fifth-order fit at energies 450 MeV and above.

The coefficients and their errors are listed for each energy and charge in Tables XIII and XIV. They are also plotted as a function of energy in Figs. 27 and 28.

Several criteria were considered in choosing the order of fit. One criterion was that if a given order were required at a certain energy, a lower order was never chosen at a higher energy. This corresponds to the fact that as the energy increases, the number of partial waves taking part in the scattering should not decrease.

An interesting test was made by comparing the fits made with and without the dispersion-relations point. In almost every case, the two fits for the chosen order were nearly identical.

Table V. Differential cross-section data for T_π = 310 MeV.

$\cos\theta^*$	$d\sigma(\theta^*)/d\Omega^*$ (mb/sr) π^+-p
1.000	14.090 ± 1.410
0.533	7.102 ± 0.330
0.450	6.391 ± 0.408
0.355	4.775 ± 0.523
0.258	2.722 ± 0.925
0.160	2.910 ± 0.621
0.045	2.071 ± 0.119
-0.067	1.646 ± 0.103
-0.174	1.447 ± 0.104
-0.308	1.402 ± 0.077
-0.472	1.699 ± 0.085
-0.613	2.163 ± 0.104
-0.720	2.818 ± 0.134
-0.800	3.549 ± 0.166
-0.860	3.962 ± 0.205
-0.903	4.214 ± 0.240
-0.946	4.786 ± 0.218

Table VI. Differential cross-section data for T_π = 370 MeV.

$\cos\theta^*$	$d\sigma(\theta^*)/d\Omega^*$ (mb/sr)	
	π^+-p	π^--p
1.000	10.040 ± 1.000	1.240 ± 0.120
0.584	5.524 ± 0.160	1.305 ± 0.044
0.510	4.845 ± 0.157	1.182 ± 0.052
0.425	4.045 ± 0.212	1.117 ± 0.075
0.328	2.933 ± 0.291	0.899 ± 0.093
0.228	1.918 ± 0.404	0.563 ± 0.114
0.130	1.744 ± 0.585	0.582 ± 0.142
0.014	1.349 ± 0.070	0.581 ± 0.026
-0.098	0.869 ± 0.056	0.447 ± 0.024
-0.204	0.653 ± 0.050	0.448 ± 0.024
-0.336	0.596 ± 0.036	0.389 ± 0.016
-0.496	0.629 ± 0.038	0.429 ± 0.018
-0.632	0.910 ± 0.050	0.506 ± 0.022
-0.735	1.219 ± 0.065	0.650 ± 0.027
-0.811	1.448 ± 0.081	0.740 ± 0.034
-0.868	1.848 ± 0.098	0.823 ± 0.041
-0.908	1.995 ± 0.113	0.933 ± 0.050
-0.949	2.199 ± 0.108	1.000 ± 0.043

Table VII. Differential cross-section data for T_π = 410 MeV.

$\cos\theta^*$	$d\sigma/d\Omega^*$ (mb/sr)	
	π^+-p	π^--p
1.000	8.150 ±0.810	1.710 ±0.170
0.639	5.423 ±0.116	1.542 ±0.039
0.571	4.375 ±0.119	1.383 ±0.044
0.495	3.841 ±0.142	1.264 ±0.065
0.408	3.199 ±0.218	1.192 ±0.089
0.310	2.065 ±0.254	0.928 ±0.094
0.209	1.342 ±0.370	0.651 ±0.125
0.110	1.361 ±0.363	0.661 ±0.117
-0.006	0.923 ±0.052	0.531 ±0.026
-0.118	0.551 ±0.038	0.406 ±0.023
-0.223	0.364 ±0.036	0.372 ±0.021
-0.353	0.279 ±0.025	0.358 ±0.015
-0.511	0.284 ±0.029	0.389 ±0.017
-0.644	0.507 ±0.036	0.528 ±0.022
-0.744	0.773 ±0.044	0.680 ±0.028
-0.818	0.912 ±0.055	0.765 ±0.034
-0.873	1.034 ±0.066	0.856 ±0.044
-0.912	1.156 ±0.077	1.050 ±0.051
-0.951	1.137 ±0.070	1.149 ±0.047

Table VIII. Differential cross-section data for T_π = 450 MeV.

$\cos\theta^*$	$d\sigma/d\Omega^*$ (mb/sr)	
	π^+-p	π^--p
1.000	6.520 ±0.650	2.540 ±0.250
0.628	4.386 ±0.092	1.594 ±0.041
0.558	3.552 ±0.094	1.494 ±0.046
0.480	3.090 ±0.126	1.412 ±0.078
0.392	2.483 ±0.150	1.190 ±0.088
0.292	1.844 ±0.201	0.980 ±0.107
0.191	1.070 ±0.306	0.566 ±0.139
0.091	1.116 ±0.243	0.670 ±0.102
-0.025	0.634 ±0.040	0.426 ±0.026
-0.136	0.351 ±0.032	0.380 ±0.022
-0.241	0.201 ±0.027	0.276 ±0.021
-0.370	0.104 ±0.019	0.255 ±0.015
-0.525	0.186 ±0.019	0.355 ±0.018
-0.655	0.268 ±0.025	0.496 ±0.023
-0.752	0.357 ±0.032	0.717 ±0.030
-0.824	0.534 ±0.040	0.917 ±0.039
-0.877	0.602 ±0.046	1.077 ±0.047
-0.915	0.599 ±0.059	1.197 ±0.059
-0.953	0.689 ±0.051	1.161 ±0.053

Table IX. Differential cross-section data for T_π = 490 MeV.

$\cos\theta^*$	$d\sigma/d\Omega^*$ (mb/sr)	
	π^+-p	π^--p
1.000	5.170±0.520	3.570 ±0.360
0.685	3.701± 0.091	1.866 ±0.057
0.617	3.751± 0.079	1.879 ±0.046
0.545	2.960± 0.080	1.558 ±0.051
0.466	2.471± 0.112	1.433 ±0.089
0.376	2.140± 0.131	1.286 ±0.097
0.276	1.279± 0.179	0.941 ±0.118
0.173	0.819± 0.220	0.620 ±0.127
0.073	0.645± 0.310	0.494 ±0.165
-0.043	0.419± 0.042	0.498 ±0.030
-0.154	0.243± 0.028	0.288 ±0.023
-0.258	0.093± 0.024	0.255 ±0.020
-0.386	0.061± 0.016	0.235 ±0.015
-0.538	0.100± 0.019	0.321 ±0.018
-0.665	0.169± 0.021	0.589 ±0.026
-0.760	0.241± 0.028	0.781 ±0.034
-0.830	0.342± 0.031	1.009 ±0.043
-0.881	0.402± 0.038	1.101 ±0.057
-0.918	0.378± 0.047	1.292 ±0.064
-0.954	0.353± 0.041	1.513 ±0.058

Table X. Differential cross-section data for T_π = 550 MeV.

Cos θ^*	$d\sigma/d\Omega^*$ (mb/sr)	
	π^+-p	π^--p
1.000	3.850 ± 0.380	5.410 ± 0.540
0.728	3.046 ± 0.068	2.951 ± 0.075
0.671	2.792 ± 0.065	2.702 ± 0.071
0.600	2.661 ± 0.055	2.422 ± 0.057
0.526	2.192 ± 0.060	2.061 ± 0.063
0.445	1.771 ± 0.078	1.634 ± 0.082
0.354	1.403 ± 0.085	1.419 ± 0.095
0.251	0.923 ± 0.121	1.014 ± 0.124
0.148	0.523 ± 0.184	0.567 ± 0.175
0.047	0.418 ± 0.194	0.413 ± 0.183
-0.070	0.299 ± 0.026	0.189 ± 0.031
-0.180	0.154 ± 0.020	0.161 ± 0.023
-0.283	0.067 ± 0.018	0.133 ± 0.022
-0.408	0.053 ± 0.014	0.190 ± 0.016
-0.556	0.104 ± 0.014	0.406 ± 0.022
-0.679	0.138 ± 0.016	0.724 ± 0.031
-0.771	0.152 ± 0.020	1.031 ± 0.040
-0.838	0.155 ± 0.023	1.219 ± 0.056
-0.887	0.146 ± 0.027	1.394 ± 0.065
-0.922	0.125 ± 0.032	1.832 ± 0.084
-0.957	0.133 ± 0.026	1.696 ± 0.075

Table XI. Differential cross-section data for T_π = 600 MeV.

$\cos\theta^*$	$d\sigma/d\Omega^*$ (mb/sr)	
	π^+-p	π^--p
1.000	2.890 ±0.290	6.930 ±0.690
0.718	2.340 ±0.055	3.778 ±0.088
0.659	2.118 ±0.052	3.289 ±0.082
0.586	1.994 ±0.044	2.995 ±0.069
0.511	1.576 ±0.050	2.462 ±0.075
0.428	1.406 ±0.068	1.888 ±0.087
0.335	1.041 ±0.071	1.449 ±0.097
0.231	0.669 ±0.097	1.037 ±0.133
0.127	0.419 ±0.167	0.569 ±0.238
0.026	0.384 ±0.105	0.356 ±0.156
-0.090	0.200 ±0.022	0.207 ±0.029
-0.200	0.108 ±0.019	0.081 ±0.023
-0.302	0.068 ±0.019	0.103 ±0.024
-0.425	0.043 ±0.016	0.185 ±0.022
-0.570	0.091 ±0.016	0.449 ±0.026
-0.691	0.182 ±0.018	0.640 ±0.034
-0.779	0.151 ±0.020	0.950 ±0.045
-0.844	0.135 ±0.022	1.028 ±0.053
-0.891	0.107 ±0.024	1.155 ±0.064
-0.925	0.126 ±0.027	1.216 ±0.079
-0.958	0.082 ±0.027	1.340 ±0.072

Table XII. Differential cross-section data for T_π = 650 MeV.

$\cos\theta^*$	$d\sigma/d\Omega^*$ (mb/sr)	
	π^+-p	π^--p
1.000	2.340 ±0.230	6.430 ±0.640
0.708	1.786 ±0.046	3.170 ±0.085
0.648	1.599 ±0.047	2.756 ±0.081
0.573	1.590 ±0.039	2.379 ±0.064
0.496	1.301 ±0.048	1.951 ±0.077
0.412	1.048 ±0.058	1.444 ±0.086
0.317	0.795 ±0.064	1.228 ±0.096
0.212	0.496 ±0.087	0.833 ±0.125
0.107	0.240 ±0.104	0.252 ±0.155
0.006	0.168 ±0.143	0.155 ±0.226
-0.110	0.111 ±0.023	0.171 ±0.033
-0.219	0.009 ±0.019	0.153 ±0.025
-0.320	0.072 ±0.018	0.204 ±0.027
-0.441	0.128 ±0.016	0.343 ±0.024
-0.584	0.158 ±0.018	0.618 ±0.032
-0.701	0.171 ±0.020	0.676 ±0.039
-0.787	0.233 ±0.021	0.820 ±0.045
-0.850	0.207 ±0.023	0.797 ±0.050
-0.895	0.151 ±0.028	0.650 ±0.059
-0.928	0.121 ±0.029	0.763 ±0.064
-0.960	0.125 ±0.027	0.755 ±0.058

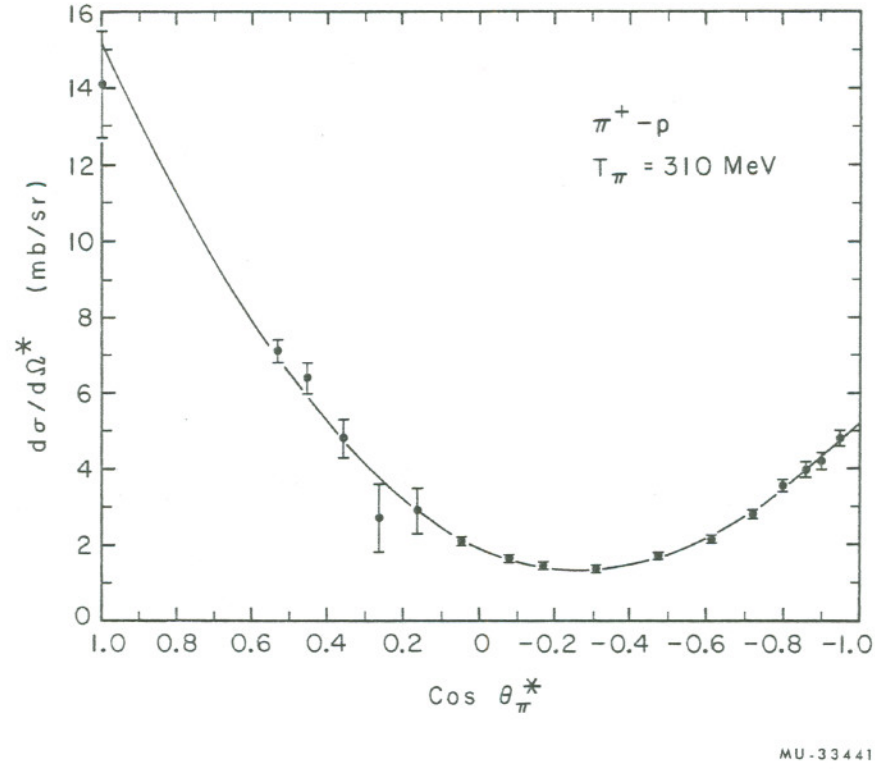

Fig. 12. Differential-cross-section data and fitted curve for $T_\pi = 310$ MeV (π^+-p).

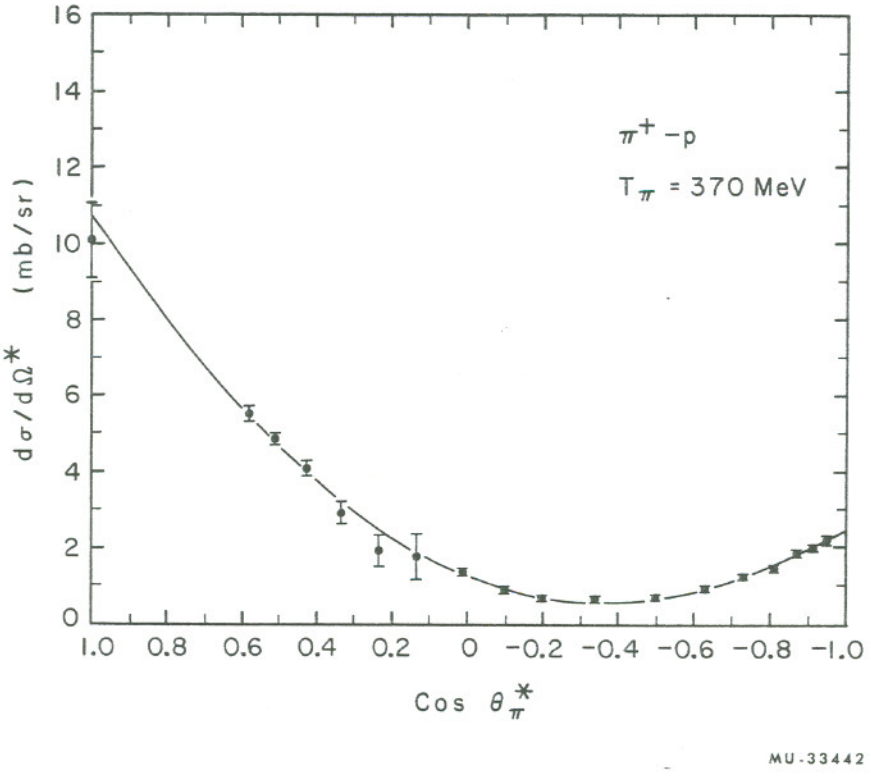

Fig. 13. Differential-cross-section data and fitted curve for T_π = 370 MeV (π^+-p).

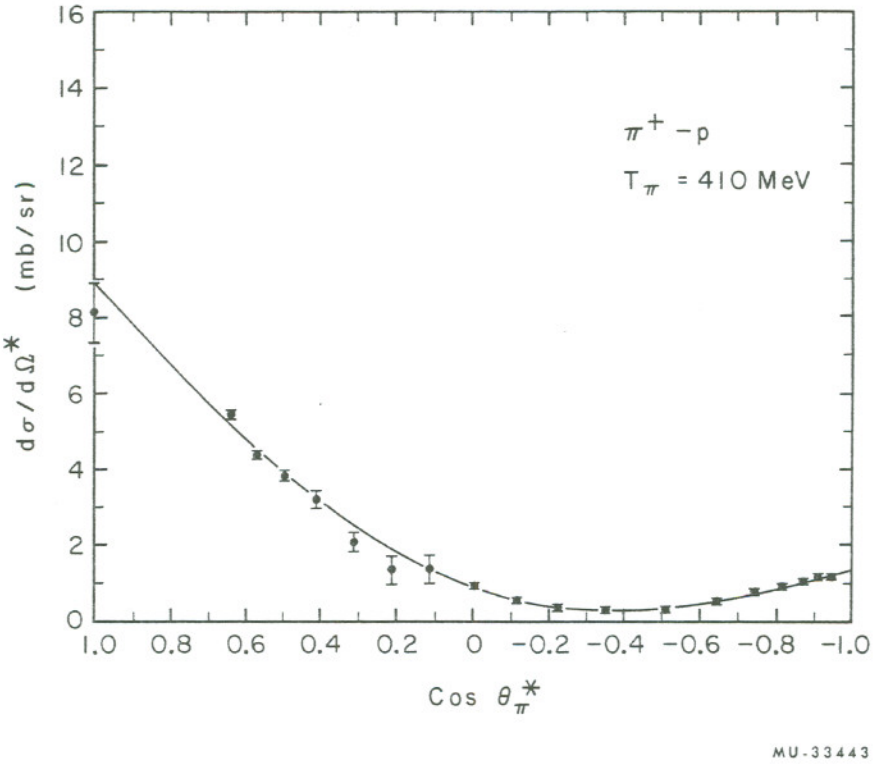

Fig. 14. Differential-cross-section data and fitted curve for T_π = 410 MeV (π^+-p).

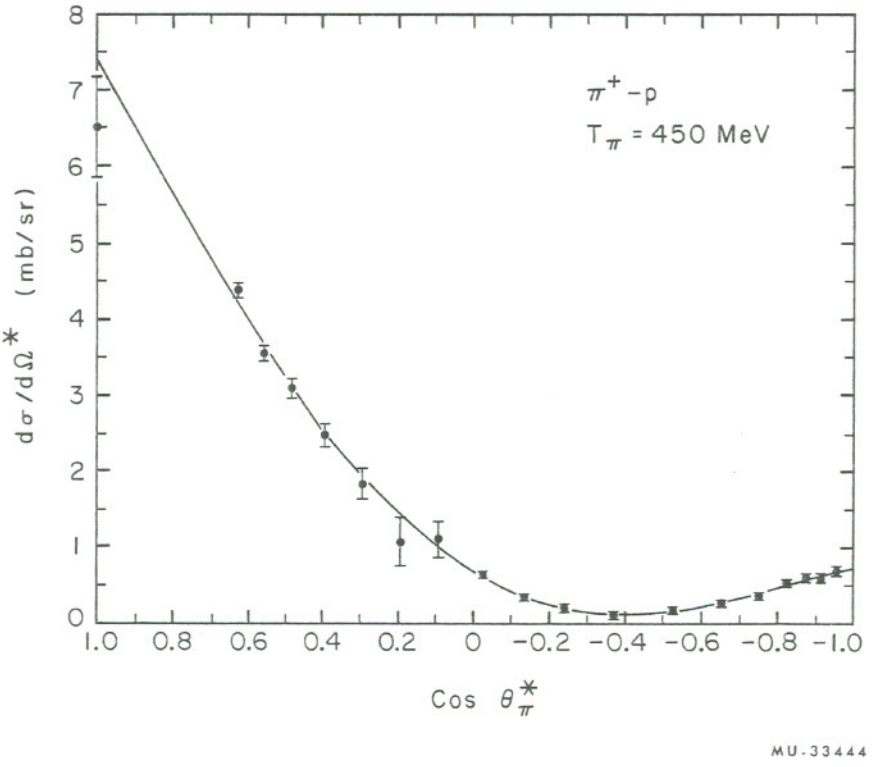

Fig. 15. Differential-cross-section data and fitted curve for T_π = 450 MeV (π^+-p).

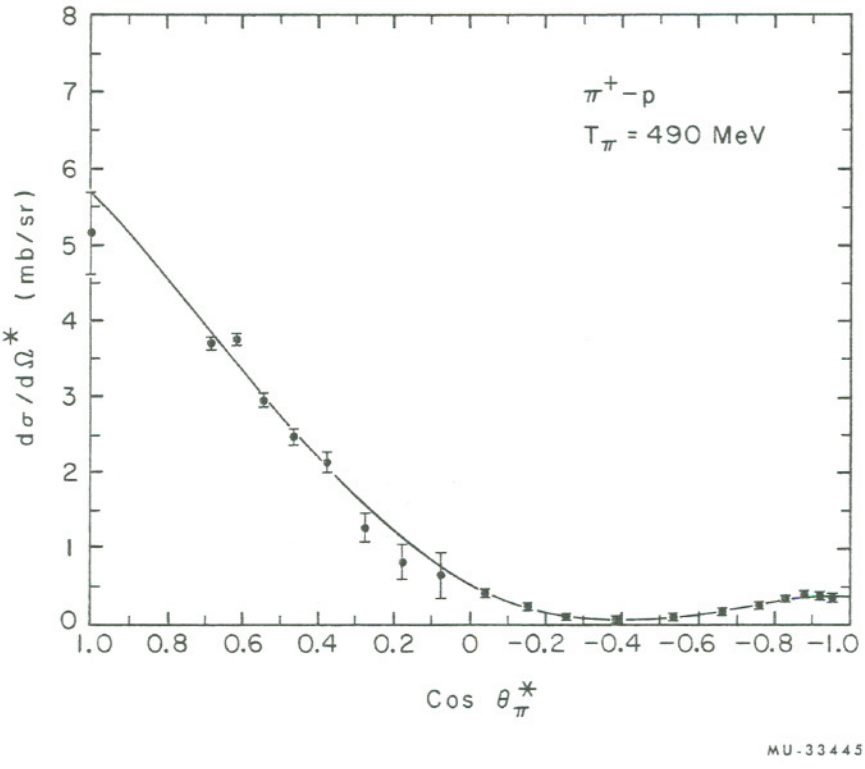

Fig. 16. Differential-cross-section data and fitted curve for T_π = 490 MeV (π^+-p).

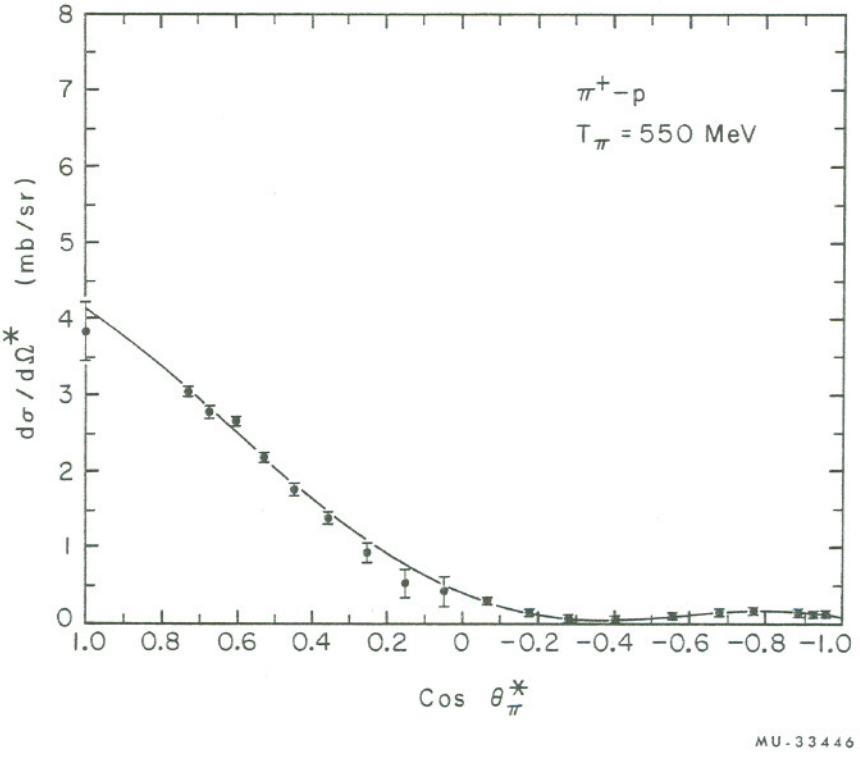

Fig. 17. Differential-cross-section data and fitted curve for T_π = 550 MeV (π^+-p).

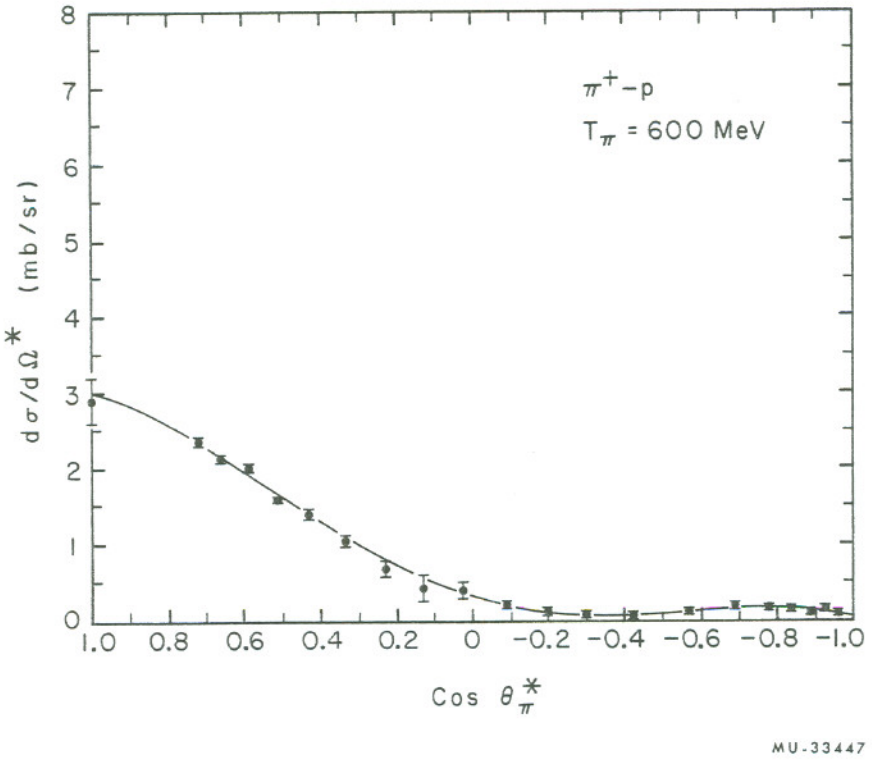

Fig. 18. Differential-cross-section data and fitted curve for T_π = 600 MeV (π^+-p).

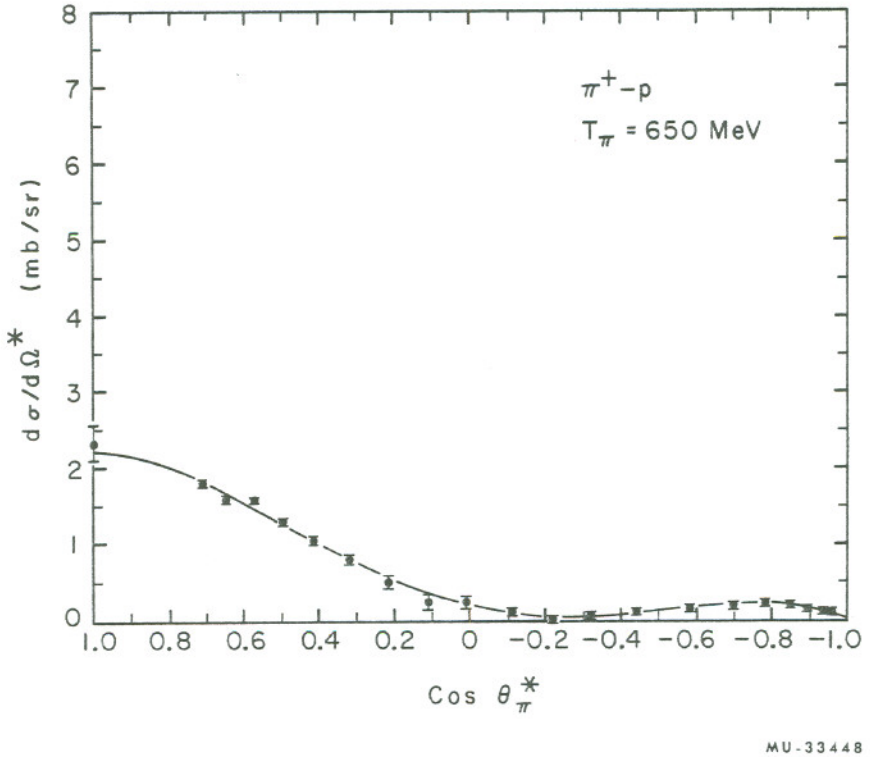

Fig. 19. Differential-cross-section data and fitted curve for T_π = 650 MeV (π^+-p).

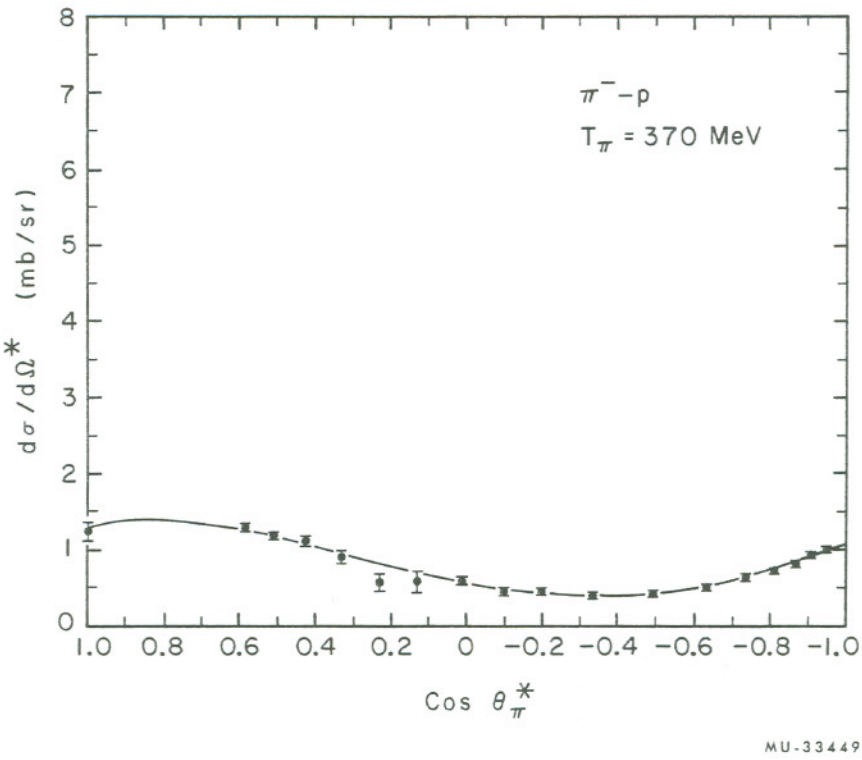

Fig. 20. Differential-cross-section data and fitted curve for T_π = 370 MeV (π^--p).

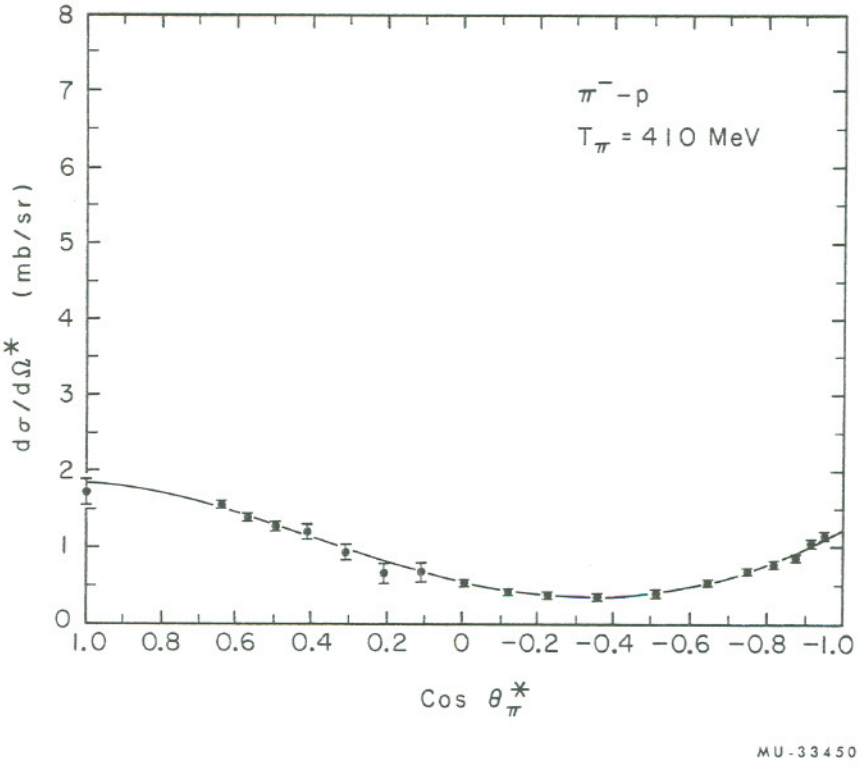

Fig. 21. Differential-cross-section data and fitted curve for T_π = 410 MeV (π^--p).

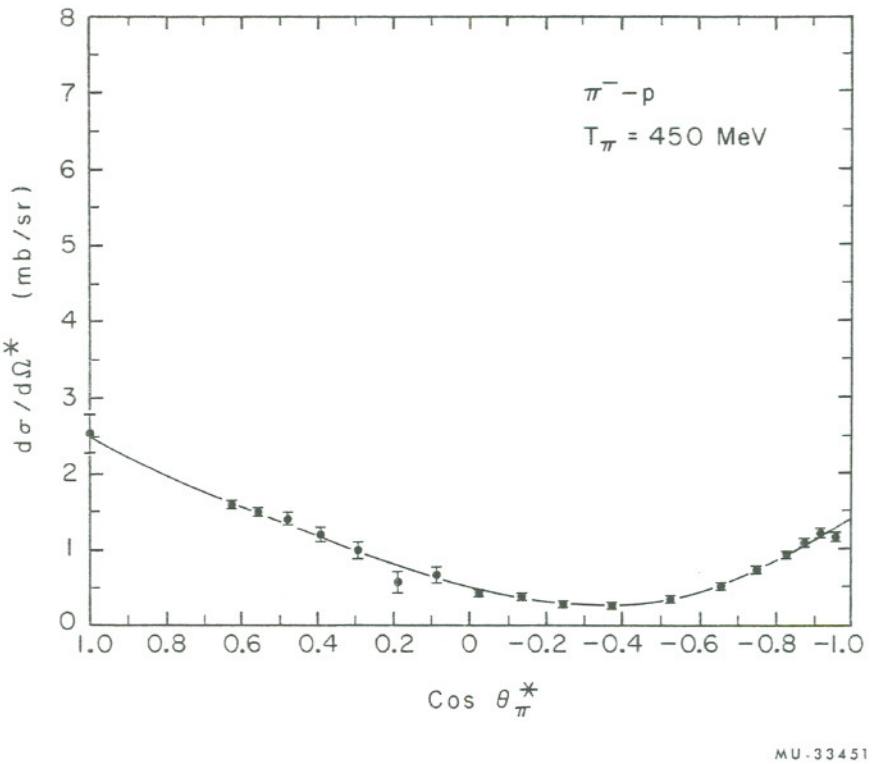

Fig. 22. Differential-cross-section data and fitted curve for T_π = 450 MeV (π^--p).

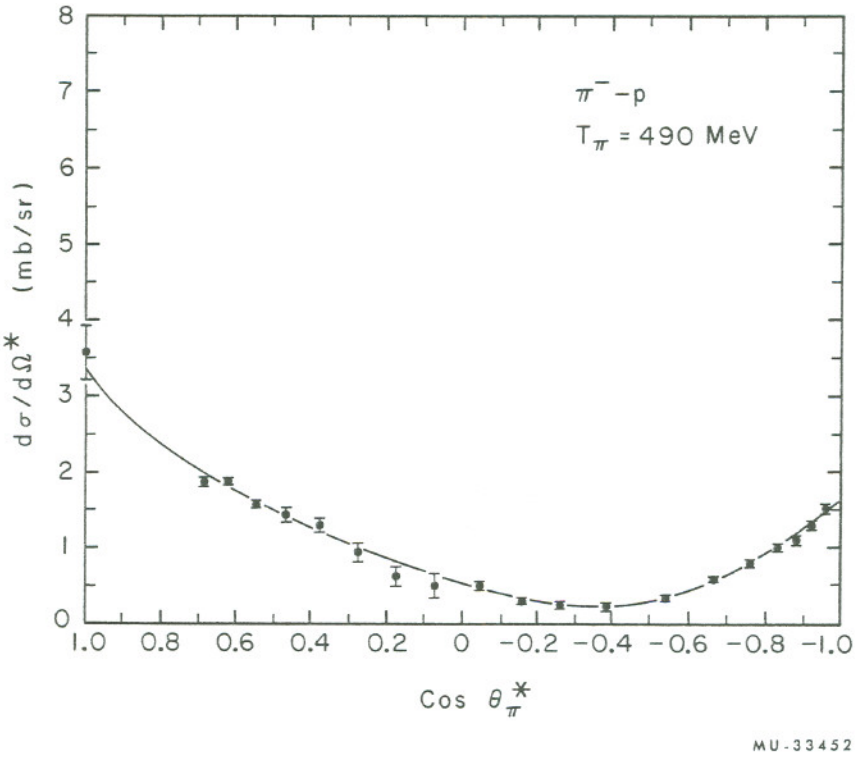

Fig. 23. Differential-cross-section data and fitted curve for T_π = 490 MeV (π^--p).

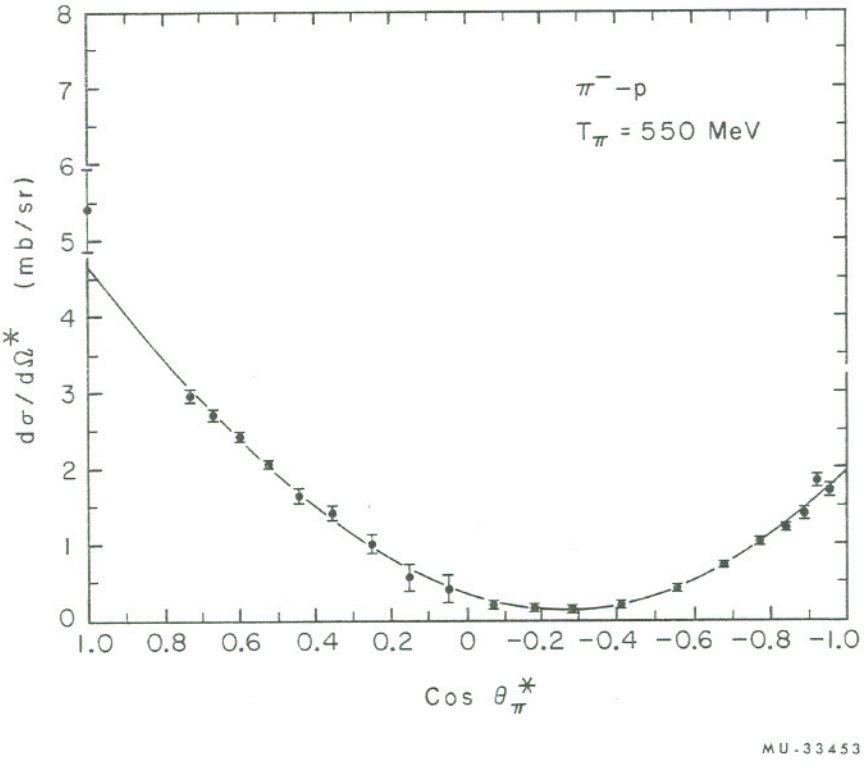

Fig. 24. Differential-cross-section data and fitted curve for T_π = 550 MeV (π^--p).

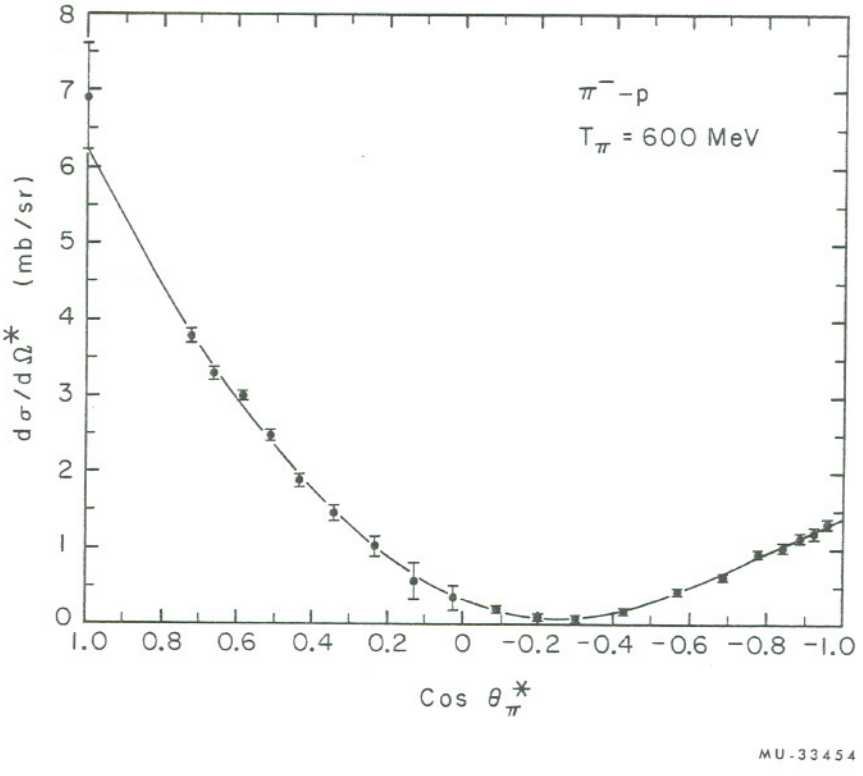

Fig. 25. Differential-cross-section data and fitted curve for T_π = 600 MeV (π^--p).

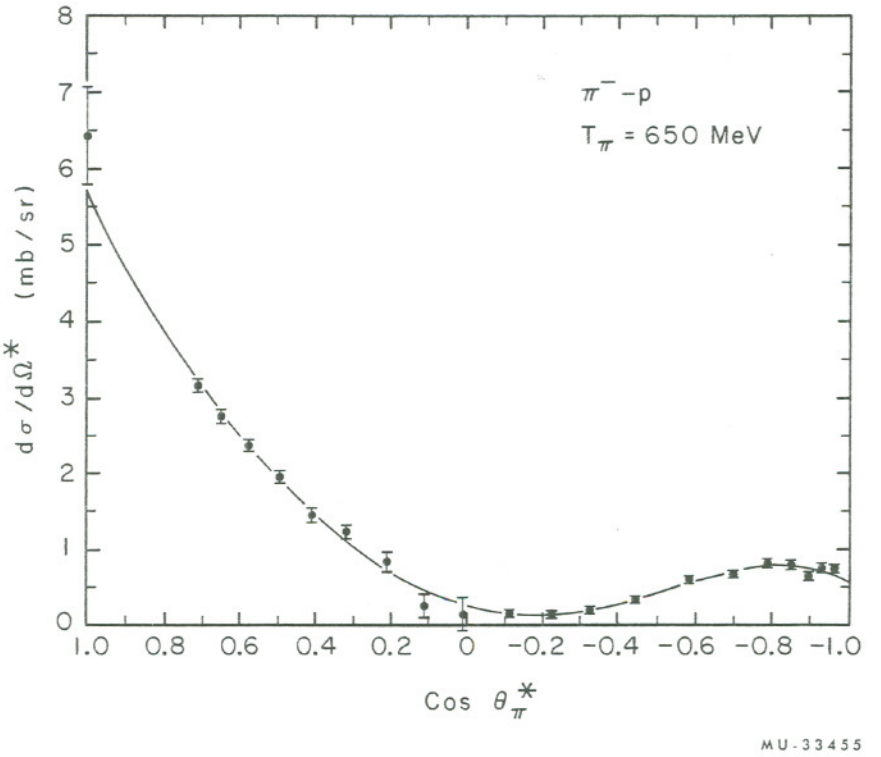

Fig. 26. Differential-cross-section data and fitted curve for T_π = 650 MeV (π^--p).

Table XIII. Coefficients of powers of $\cos\theta^*$ (π^+-p).

	Pion kinetic energy in lab system (MeV)							
a	310	370	410	450	490	550	600	650
a_0	1.958±0.051	1.256±0.031	0.905±0.036	0.691±0.026	0.554±0.034	0.412±0.017	0.312±0.015	0.207±0.022
a_1	4.697±0.253	3.968±0.140	3.558±0.167	3.038±0.118	2.692±0.138	1.988±0.068	1.546±0.060	1.192±0.070
a_2	8.925±0.472	5.670±0.209	5.112±0.218	4.260±0.147	3.771±0.171	2.960±0.088	2.446±0.087	2.348±0.118
a_3	0.297±0.644	0.193±0.416	0.249±0.458	0.305±0.329	-0.022±0.353	0.053±0.162	0.044±0.144	-0.102±0.168
a_4	-0.719±0.754	-0.314±0.440	-0.871±0.485	-0.880±0.334	-1.280±0.362	-1.272±0.171	-1.234±0.158	-1.440±0.194

a. Coefficients

Table XIV. Coefficients of powers of $\cos\theta^*$ (π^--p).

Coefficients	Pion kinetic energy in lab system (MeV)						
	370	410	450	490	550	600	650
a_0	0.561±0.014	0.537±0.013	0.497±0.021	0.518±0.029	0.347±0.029	0.343±0.024	0.274±0.034
a_1	0.964±0.045	1.092±0.045	1.316±0.092	1.501±0.115	1.718±0.112	2.039±0.094	1.371±0.121
a_2	1.076±0.098	1.285±0.085	1.371±0.139	1.347±0.194	3.095±0.218	4.081±0.193	3.914±0.263
a_3	-0.858±0.089	-0.786±0.104	-1.220±0.377	-1.425±0.469	-0.501±0.485	-0.041±0.405	0.332±0.523
a_4	-0.449±0.126	-0.290±0.134	0.080±0.233	0.621±0.352	0.138±0.390	-0.608±0.360	-1.057±0.469
a_5	--	--	0.460±0.361	0.773±0.495	0.117±0.558	0.439±0.482	0.847±0.609

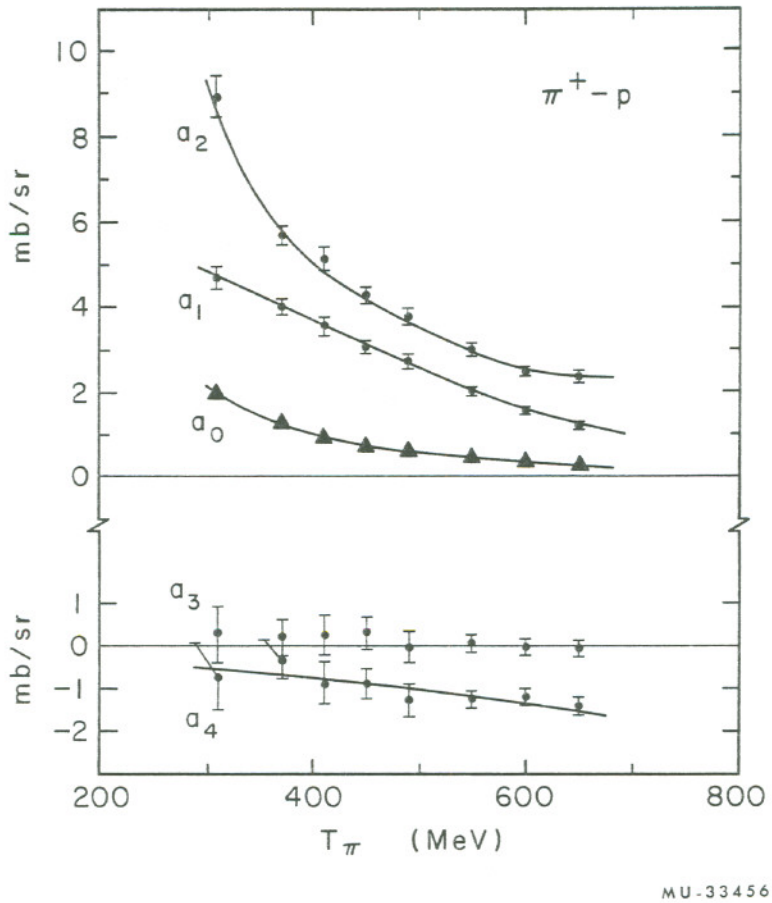

Fig. 27. Coefficients of powers of $\cos\theta_\pi^*$ plotted vs pion energy (π^+-p).

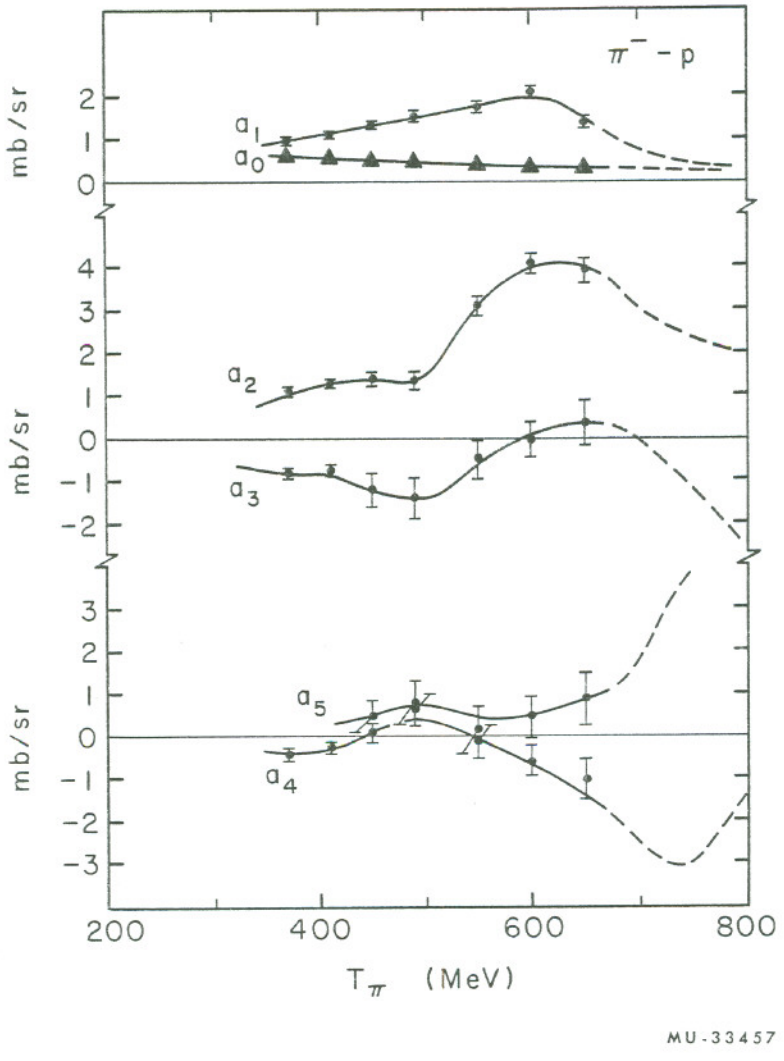

Fig. 28. Coefficients of powers of $\cos\theta_\pi^*$ plotted vs pion energy (π^--p). The dashed lines show the higher energy behavior as indicated by the results of Helland et al.[5]

An important consideration was the standard χ^2 test. The goodness-of-fit parameter, $(\chi^2/d)^{1/2}$, for which d is the number of degrees of freedom, was calculated for each order. The chosen order was the lowest one for which an increase in the order gave little or no change in the goodness-of-fit parameter. Except for a few cases for which the other previously mentioned criteria indicated strongly that a higher order was needed, the χ^2 test selected the order of fit.

In Table XV for π^+-p and Table XVI for π^--p, the goodness-of-fit parameter, the order of fit, and the number of degrees of freedom are listed for each energy.

C. Total Elastic Cross Sections

By integrating under the fitted differential-cross-section curves, measurements of the total elastic cross section were obtained. These values and their errors are listed in Table XVII and plotted as a function of energy in Fig. 29.

Table XV. Order of fit (N), degrees of freedom (d), and goodness-of-fit $(\chi^2/d)^{1/2}$ parameter at each energy (π^+-p).

Energy	N	d	$(\chi^2/d)^{1/2}$
310	4	12	0.788
370	4	13	0.793
410	4	14	1.174
450	4	14	1.051
490	4	15	1.442
550	4	16	1.032
600	4	16	1.077
650	4	16	1.438

Table XVI. Order of fit (N), degrees of freedom (d), and goodness-of-fit $(\chi^2/d)^{1/2}$ parameter at each energy (π^--p).

Energy	N	d	$(\chi^2/d)^{1/2}$
370	4	13	0.991
410	4	14	0.911
450	5	13	1.124
490	5	14	1.301
550	5	15	1.158
600	5	15	0.878
650	5	15	1.123

Table XVII. Total elastic cross sections from integration of differential cross sections.

Energy	$\sigma_{tot\ el}$ (mb)	
	π^+-p	π^--p
310	60.19 ± 1.41	--
370	38.74 ± 0.73	10.42 ± 0.17
410	30.59 ± 0.66	11.40 ± 0.16
450	24.31 ± 0.49	12.19 ± 0.26
490	19.55 ± 0.46	13.71 ± 0.35
550	14.38 ± 0.19	16.98 ± 0.37
600	11.06 ± 0.18	19.87 ± 0.34
650	8.82 ± 0.22	17.19 ± 0.45

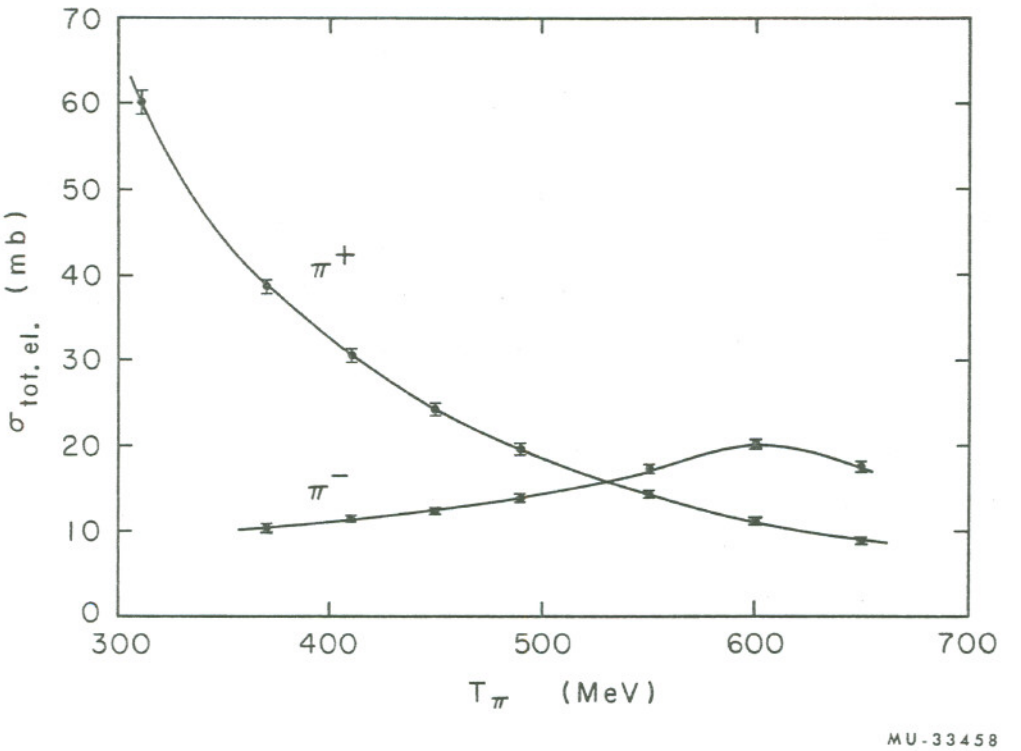

Fig. 29. Total elastic cross sections plotted vs pion energy.

V. DISCUSSION

A. Partial-Wave Equations

In this experiment, 280 differential cross-section measurements were made. The average statistical error on these measurements is between 3 and 3.5 percent. These data serve to define quite accurately the angular distributions for pion-proton elastic scattering from 300 to 700 MeV.

In Sec. I a number of other experiments were mentioned in which differential cross-section measurements in the 300 to 700 MeV range were made. The 310-MeV π^+-p data (Fig. 12) of this experiment were taken primarily to check the agreement between the measurements of this experiment and the more extensive measurements of Foote et al.[4b] at that energy. The agreement is very good.

At the high-energy end of the range, the agreement is also very good between the measurements of this experiment and those of Helland et al.[5a] and Wood et al.[5b]

Because of the low statistical accuracy of the other experiments performed in this range,[6] comparison with these experiments has little significance.

In order to understand the π-N interaction better, it is of interest to know how the various angular-momentum states participate in the scattering. Particularly, one would like to know what states, if any, are dominant.

One approach to this problem is a close examination of the behavior, as a function of energy, of the coefficients of a cosine power-series expansion of the differential cross section. In order to do this, it will first be necessary to present the partial-wave equations and define the notation to be used.

The partial-wave expansion of the differential cross section for a spinless particle (pion) and a spin-1/2 particle (proton) is

$$\frac{d\sigma(\theta^*)}{d\Omega^*} = \left| \sum_{\ell=0}^{\infty} [(\ell+1) A_\ell^+ + \ell A_\ell^-] P_\ell(\cos\theta^*) \right|^2 + \left| \sum_{\ell=1}^{\infty} (A_\ell^+ - A_\ell^-) P_\ell^1(\cos\theta^*) \right|^2. \tag{22}$$

The index ℓ represents the orbital angular-momentum state, whereas + and - superscripts indicate that the total angular momentum J is $\ell + 1/2$ or $\ell - 1/2$, respectively. The function $P_\ell(\cos\theta^*)$ and $P_\ell^1(\cos\theta^*)$ are the Legendre polynomial and first associated Legendre polynomial of order ℓ, respectively. The partial-wave scattering amplitude $A_\ell^\pm$ can be written as a function of the real part of the phase shift $\delta_\ell^\pm$, the absorption parameter $\eta_\ell^\pm$, and the c.m. wave number k.

$$A_\ell^\pm = \frac{\eta_\ell^\pm \exp(2i\delta_\ell^\pm) - 1}{2ik} . \tag{23}$$

When plotted in the complex plane, the amplitude kA lies within a circle of radius 1/2 and centered on the imaginary axis at + 1/2, as shown in Fig. 30. The parameters δ and η are also shown in Fig. 30.

In the expansion of the differential cross section the interference between two states with amplitudes A_i and A_j appears in the form $\mathrm{Re}(A_i^* A_j)$. This term can also be written as

$$\mathrm{Re}\,(A_i^* A_j) = |A_i||A_j| \cos\alpha. \tag{24}$$

where α is the angle between the two amplitudes as shown in Fig. 30. Thus, we see that the sign of an interference term changes as the angle between the two amplitudes passes through 90 deg.

Another notation for the partial-wave amplitudes is commonly used. The form is $(\ell \text{ state})_J$, with the ℓ state being represented by the familiar spectroscopic notation S, P, D, F, etc. In this notation, for example, the amplitude A_2^- would be given the symbol $D_{3/2}$.

If the summations in Eq. (22) are cut off at a value ℓ_{max}, that expression can be expanded and the terms recombined in the form,

$$\frac{d\sigma(\theta^*)}{d\Omega^*} = \sum_{n=0}^{2\ell_{max}} a_n \cos^n\theta^*, \tag{25}$$

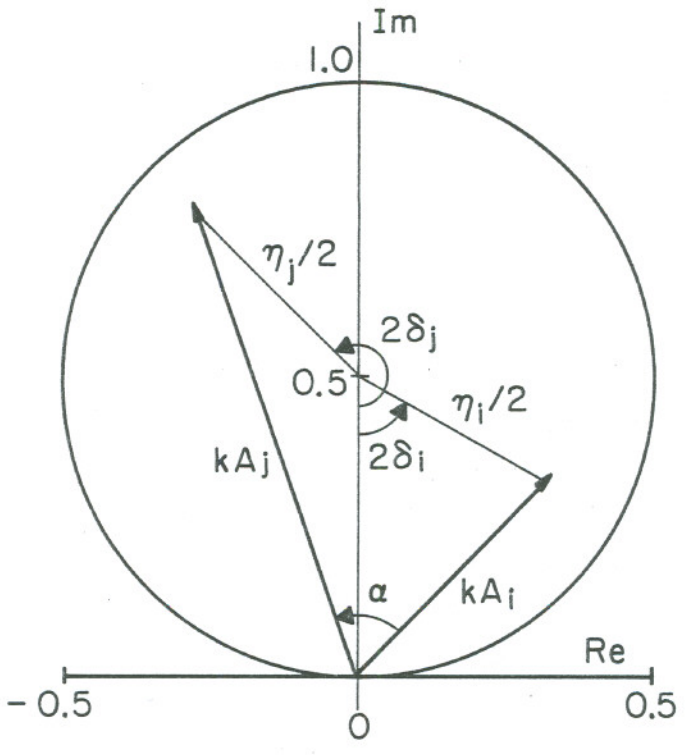

Fig. 30. Diagrams showing scattering amplitudes plotted in the complex plane.

where

$$a_n = \sum_{i=1}^{2\ell_{max}+1} \sum_{\substack{j=1 \\ j\geq i}}^{2\ell_{max}+1} c_{nij}\, \mathrm{Re}(A_i^* A_j) \,. \qquad (26)$$

For the case when $\ell_{max} = 3$, the coefficient c_{nij} are given in Table XVIII. Thus, from this table we see that when $\ell_{max} = 3$,

$$a_6 = (525/2)\, \mathrm{Re}(F_{5/2}^{*}\, F_{7/2}) + (175/4) \left| F_{7/2} \right|^2 . \qquad (27)$$

At this point, it is necessary to introduce a third notation for the partial-wave amplitudes. This need arises from the introduction of the isotopic spin T. The most common notation, designating isotopic spin, is of the form $(\ell \text{ state})_{2T,\,2J}$. Thus the $D_{3/2}$ amplitude in the $T = 1/2$ isotopic-spin state would have the symbol D_{13}.

We know that π^+-p is a pure $T = 3/2$ isotopic-spin state, whereas π^--p is a mixture, 1/3 (T=3/2) and 2/3 (T=1/2). Using again the $D_{3/2}$ amplitude as an example, we can write for π^+-p,

$$D_{3/2} \equiv D_{33} \,, \qquad (28)$$

whereas, for π^--p,

$$D_{3/2} \equiv (1/3) D_{33} + (2/3)\, D_{13} \,. \qquad (29)$$

B. Interpretation of π^+-p Results

Now that the groundwork for our discussion has been laid, we will proceed to the actual physical situation. Consider first the π^+-p coefficients, plotted vs energy in Fig. 27. The smooth behavior of the coefficients indicates that little of interest is occurring in the $T = 3/2$ state in this energy range. Below 300 MeV we know that the scattering is dominated by the P_{33} amplitude, resonant at about 200 MeV.

Table XVIII. Coefficients for representation of cosine power-series coefficients in terms of partial-wave amplitudes (see test).

		$S_{1/2}$	$P_{1/2}$	$P_{3/2}$	$D_{3/2}$	$D_{5/2}$	$F_{5/2}$	$F_{7/2}$
a_0	$S_{1/2}$	1			-2	-3		
	$P_{1/2}$		1	-2			-3	3
	$P_{3/2}$			1			3	-3
	$D_{3/2}$				1	3		
	$D_{5/2}$					9/4		
	$F_{5/2}$						9/4	-9/2
	$F_{7/2}$							9/4
a_1	$S_{1/2}$		2	4			-9	-12
	$P_{1/2}$				4	-9		
	$P_{3/2}$				-10			
	$D_{3/2}$							21
	$D_{5/2}$						45/2	9
	$F_{5/2}$							
	$F_{7/2}$							
a_2	$S_{1/2}$				6	9		
	$P_{1/2}$			6			9	-30
	$P_{3/2}$			3			-36	-6
	$D_{3/2}$				3	-36		
	$D_{5/2}$					-9/2		
	$F_{5/2}$						-9/2	207/2
	$F_{7/2}$							45/4
a_3	$S_{1/2}$						15	20
	$P_{1/2}$					15		
	$P_{3/2}$				18	12		
	$D_{3/2}$						12	-110
	$D_{5/2}$						-117	-30
	$F_{5/2}$							
	$F_{7/2}$							
a_4	$S_{1/2}$							
	$P_{1/2}$							35
	$P_{3/2}$						45	25
	$D_{3/2}$					45		
	$D_{5/2}$					45/4		
	$F_{5/2}$						45/4	-675/2
	$F_{7/2}$							-165/4
a_5	$S_{1/2}$							
	$P_{1/2}$							
	$P_{3/2}$							
	$D_{3/2}$							105
	$D_{5/2}$						225/2	45
	$F_{5/2}$							
	$F_{7/2}$							
a_6	$S_{1/2}$							
	$P_{1/2}$							
	$P_{3/2}$							
	$D_{3/2}$							
	$D_{5/2}$							
	$F_{5/2}$							525/2
	$F_{7/2}$							175/4

The smooth decrease in a_0, a_1, and a_2 in going from 300 to 700 MeV can easily be recognized as a result of the decreasing importance of the P_{33} state.

One observation regarding the D-wave phases can be made from a consideration of the coefficient a_4. Since a fifth or higher order fit was not needed, we are fairly confident that the F waves can be neglected. With this assumption, Table XVIII tells us that

$$a_4 = 45\ \mathrm{Re}(D_{33}^{*}\ D_{35}) + (45/4)\ |D_{35}|^2 . \qquad (30)$$

From Fig. 27, we see that a_4 is negative. Since the second term in Eq. (30) is positive definite, the first term must be negative. This implies that the D_{33} and D_{35} phases have opposite signs.

C. Interpretation of π^--p Results

Next, let us consider the more complex π^--p situation. The presence of both isotopic-spin states makes the interpretation of the coefficients difficult. However, we have seen that the $T = 3/2$ states are in general of small amplitude and slowly varying in this energy range.

The π^--p coefficients are plotted vs energy in Fig. 28. Considerable structure is apparent in the region around 600 MeV. A peak in both the total cross section (Fig. 1) and the total elastic cross section (Fig. 29) occurs at about 600 MeV.

Several explanations have been given for the 600-MeV enhancement. Peierls, on the basis of photoproduction measurements, ascribed the enhancement to a resonance in the D_{13} state.[16] Bareyre et al. have recently reported evidence that a D_{13} resonance is not sufficient, and that a resonance in either the S_{11} or P_{11} state may occur at about 430 MeV, in addition to a D_{13} resonance at 600 MeV.[17] Further suggestion of two resonant states is given by the recent partial-wave analysis of Roper.[18] He expanded the real and imaginary parts of the phase shifts in power series in the c.m. momentum. By means of an electronic computer he then varied the parameters to obtain a single fit to all the data

in the energy region under consideration. Roper has found a solution with a P_{11} resonance at about 500 MeV and a D_{13} resonance at about 650 MeV, both resonances being highly absorptive. However, the energy dependences assumed by Roper may not be reasonable, and no account was taken of any connection between the real and imaginary parts of the scattering amplitude. Such a connection is predicted by dispersion theory.

Neither a P_{11} nor a D_{13} resonance fits in the scheme of the Regge-pole hypothesis.[19] Furthermore, the nucleon itself is a P_{11} π-N state and one would not expect two distinct resonances with identical quantum numbers. Such theoretical difficulties and various other considerations have led many to believe that the 600-MeV enhancement is a result of inelastic processes. Ball and Frazer have pointed out that a rapidly increasing inelastic cross section may give rise to a peak in the elastic cross section.[20] Such a behavior could also be associated with certain prominent angular-momentum states.

One difficulty in ascribing the 600-MeV enhancement to inelastic processes is the preference for the $T = 1/2$ state. However, such a difficulty could be avoided if the $T = 0$, π-π state were dominant. In the case of single-pion production, the $T = 0$, π-π state can be produced from a $T = 1/2$, π-N state but not from a $T = 3/2$ state. Evidence that the $T = 0$ state of two pions is indeed predominant in low-energy π-π interactions has been pointed out by Schnitzer,[21] Kurz,[22] and Kirz et al.[23]

A few general remarks about resonances are in order. The Breit-Wigner resonance theory predicts the following form for an elastic resonant amplitude:[24]

$$kA = \frac{\Gamma_{el}}{2(E_R - E) - i\Gamma} \quad . \tag{31}$$

Here, Γ_{el} and Γ are the elastic and total widths of the resonance. The total c.m. energy is E and the resonant energy is E_R. It is convenient to introduce the notation of Watson, et al.[25]

$$x = \Gamma_{el}/\Gamma, \tag{32}$$

and

$$\epsilon = (2/\Gamma)(E_R - E). \tag{33}$$

In terms of these symbols,

$$kA = x/(\epsilon - i). \tag{34}$$

If the elasticity x is constant, the amplitude kA lies on a circle of radius x/2 as shown in Fig. 31.

In order to assess the compatibility of the data of this experiment with a D_{13} resonance, we shall assume that a D_{13} resonance with a Breit-Wigner form is present and attempt to fit the energy variation of the π^--p coefficients. Certain assumptions will be made about the other states involved. The reasonableness of these assumptions and the accuracy of the fit will determine the success of the analysis.

In this rough analysis we shall neglect the effects of the states whose amplitudes we would expect to be small--namely, the P_{13}, D_{33}, D_{35}, and F_{35} states and all states with total angular momentum $J > 5/2$. Experiments at higher energies have indicated that the F_{15} state is resonant and the D_{15} amplitude large, or vice versa, at about 900 MeV.[5] We shall assume an F_{15} resonance at 900 MeV with a Breit-Wigner form. A Breit-Wigner form for the P_{33} resonance will also be used, the width being such as to agree at 310 MeV with the partial-wave analysis of Foote, et al.[4b] The parameters x, Γ, and E_R, which we shall use for the P_{33}, D_{13}, and F_{15} resonances, are given in Table XIX. Those for the D_{13} and F_{15} states were either taken directly from or estimated from the work of Omnes and Valladas.[26] These parameters were chosen somewhat arbitrarily and should not be taken too seriously.

Table XIX. Breit-Wigner parameters assumed for P_{33}, D_{13}, and F_{15} resonances.

State	E_R	$x = \frac{\Gamma_{el}}{\Gamma}$	Γ
P_{33}	1238	1.0	165
D_{13}	1512	0.8	110
F_{15}	1688	0.9	100

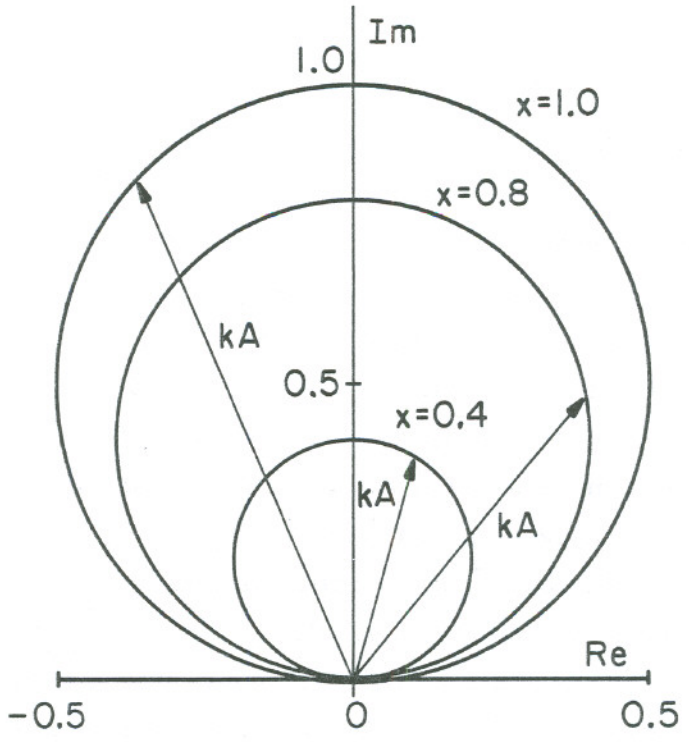

Fig. 31. Circles showing the locus of Breit-Wigner scattering amplitudes for three values of the parameter x ($x = \Gamma_{el}/\Gamma$).

The real and imaginary parts of the resonant amplitudes are plotted vs energy in Fig. 32. On the low-energy side of the D_{13} and F_{15} resonances, multiplicative factors are put in to bring the amplitudes to zero. This was necessary because of the simplifying assumption that the Γ's were constant.

The behavior assumed for the $S_{1/2}$, $P_{1/2}$, and D_{15} states is shown in Fig. 33. Motivation for the assumptions made is given in the ensuing paragraphs.

Let us now consider the coefficient a_0. The $|D_{3/2}|^2$ term gives a positive peak at 600 MeV as shown in Fig. 34. From Fig. 28 we see that no such peak appears in a_0. However, if we assume that the real part of the $S_{1/2}$ amplitude is negligibly small and that the imaginary part is constant at a value 0.27, the $S_{1/2}\,D_{3/2}$ interference term cancels the effect of the $|D_{3/2}|^2$ term. The $S_{1/2}D_{3/2}$ term is shown with the $|D_{3/2}|^2$ term in Fig. 34. The assumption of a pure imaginary S state is not unreasonable in view of the fact that the π^--p amplitude is a combination of two amplitudes. If $2\ \mathrm{Re}\ S_{11} = -\mathrm{Re}\ S_{31}$, the resultant $S_{1/2}$ amplitude for π^--p is pure imaginary.

The same two terms, $|D_{3/2}|^2$ and $S_{1/2}D_{3/2}$, which have opposite signs in a_0, have the same sign in a_2 and combine to produce a large peak as shown in Fig. 35. This is consistent with the large positive peak in a_2 shown in Fig. 28.

The general trend in the coefficient a_4 appears to be consistent with a $D_{3/2}D_{5/2}$ interference for which the $D_{5/2}$ amplitude has the form shown in Fig. 33. The contribution to a_4 from this term is plotted in Fig. 36.

The contribution to a_3 from $P_{3/2}D_{3/2}$ interference is shown in Fig. 37 together with that from $D_{5/2}F_{5/2}$ interference. These two terms give the proper trend in a_3.

The states discussed so far do not give a good prediction for the coefficient a_1. Both the $P_{3/2}D_{3/2}$ and the $D_{5/2}F_{5/2}$ terms contribute little to a_1 at 600 MeV as shown in Fig. 38. However, a 2-mb peak in a_1 is indicated by the data in Fig. 28. The only other state that could interfere with the $D_{3/2}$ and contribute to a_1 is the $P_{1/2}$ state. If we assume, as

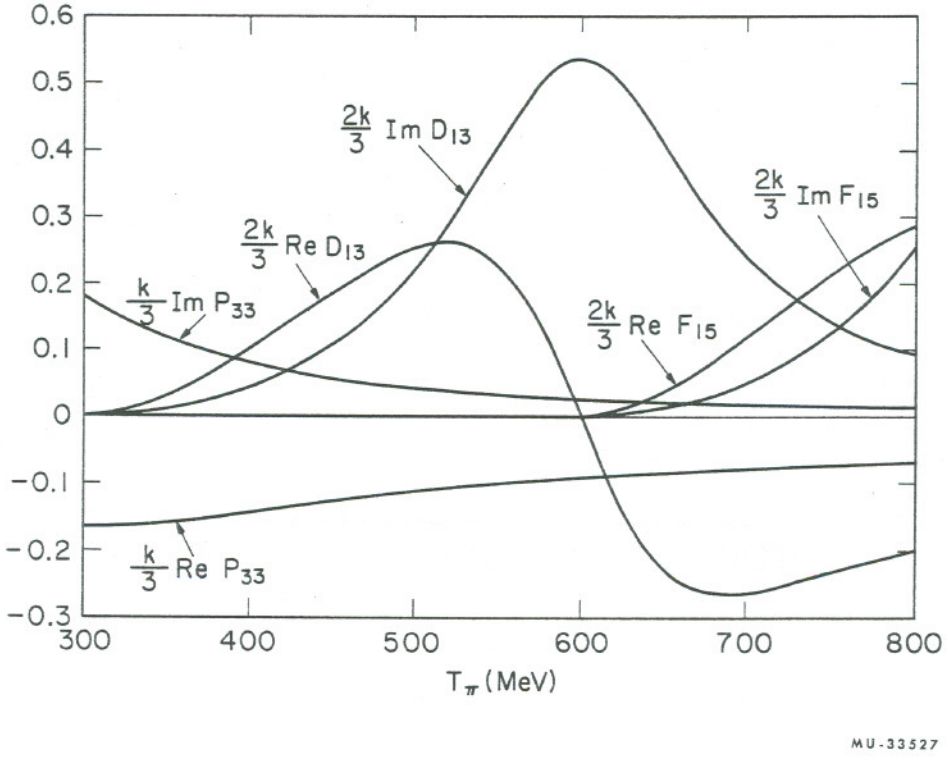

Fig. 32. Assumed resonant behavior of the P_{33}, D_{13}, and F_{15} amplitudes.

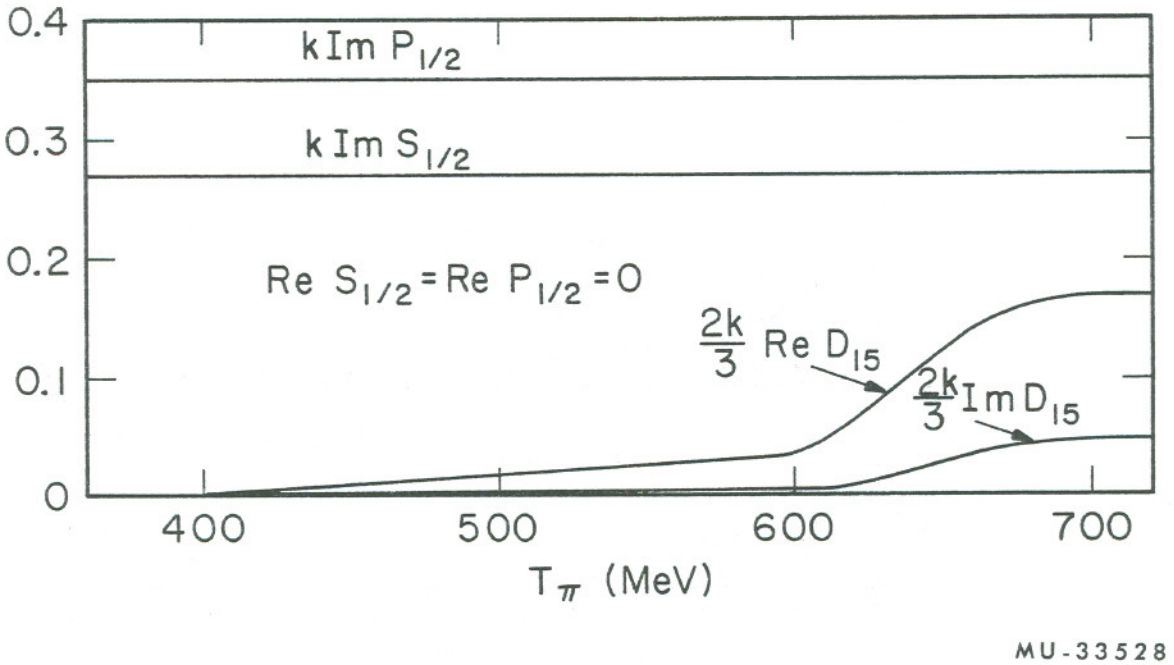

Fig. 33. Assumed behavior of the $S_{1/2}$, $P_{1/2}$, and D_{15} amplitudes.

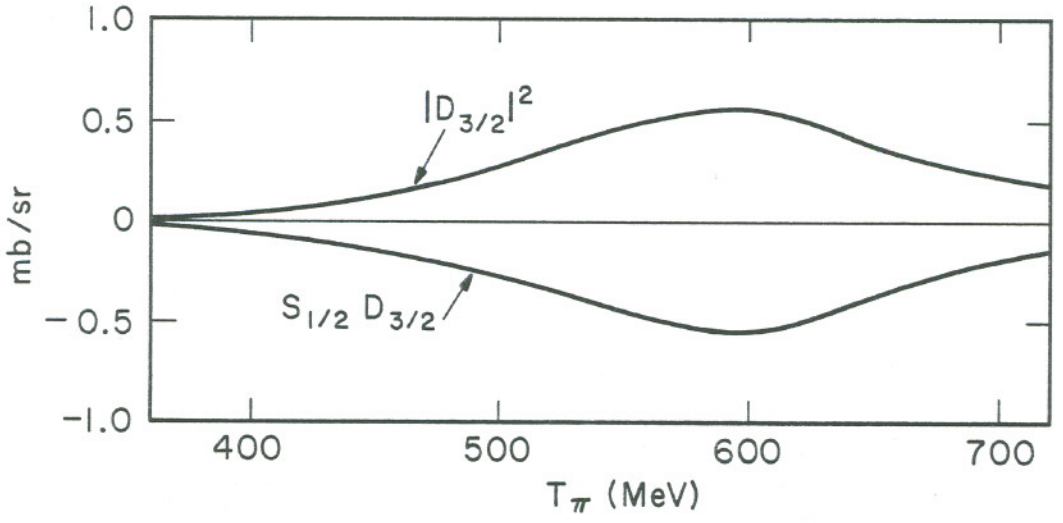

MU-33529

Fig. 34. Contribution to a_0 from $|D_{3/2}|^2$ and $S_{1/2}D_{3/2}$ terms.

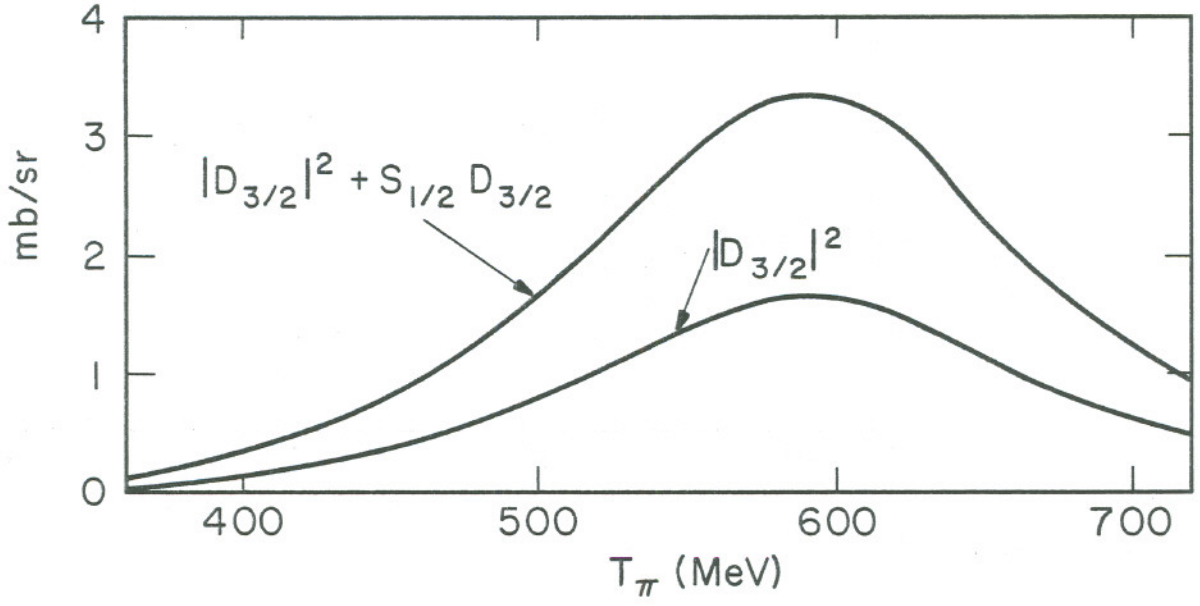

Fig. 35. Contribution to a_2 from $|D_{3/2}|^2$ and $S_{1/2} D_{3/2}$ terms.

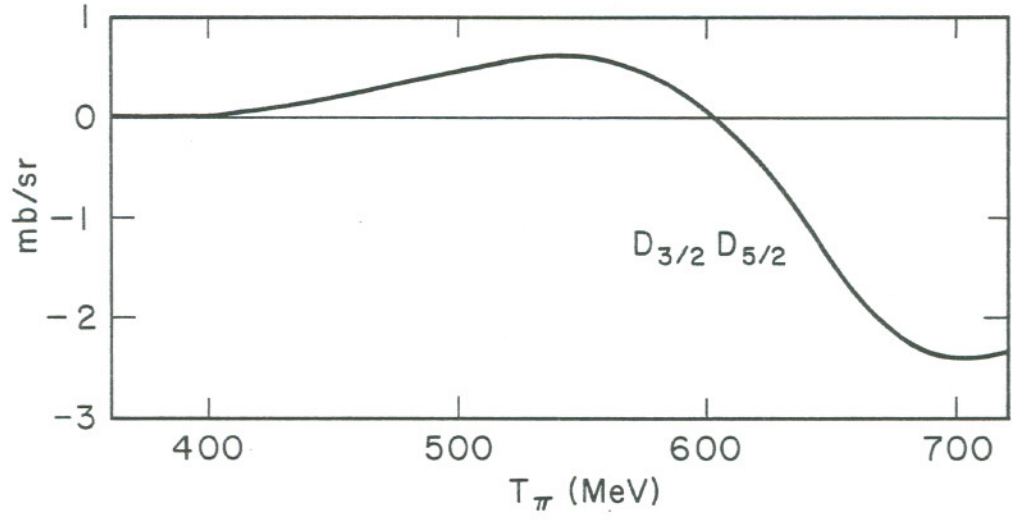

Fig. 36. Contribution to a_4 from $D_{3/2}D_{5/2}$ term.

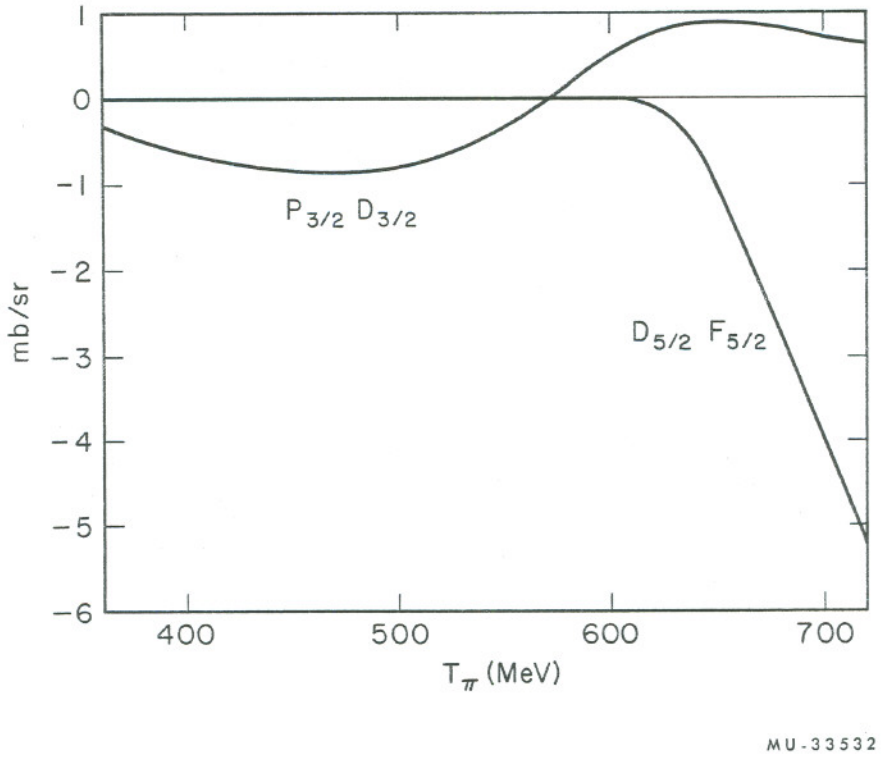

Fig. 37. Contribution to a_3 from $P_{3/2}D_{3/2}$ and $D_{5/2}F_{5/2}$ terms.

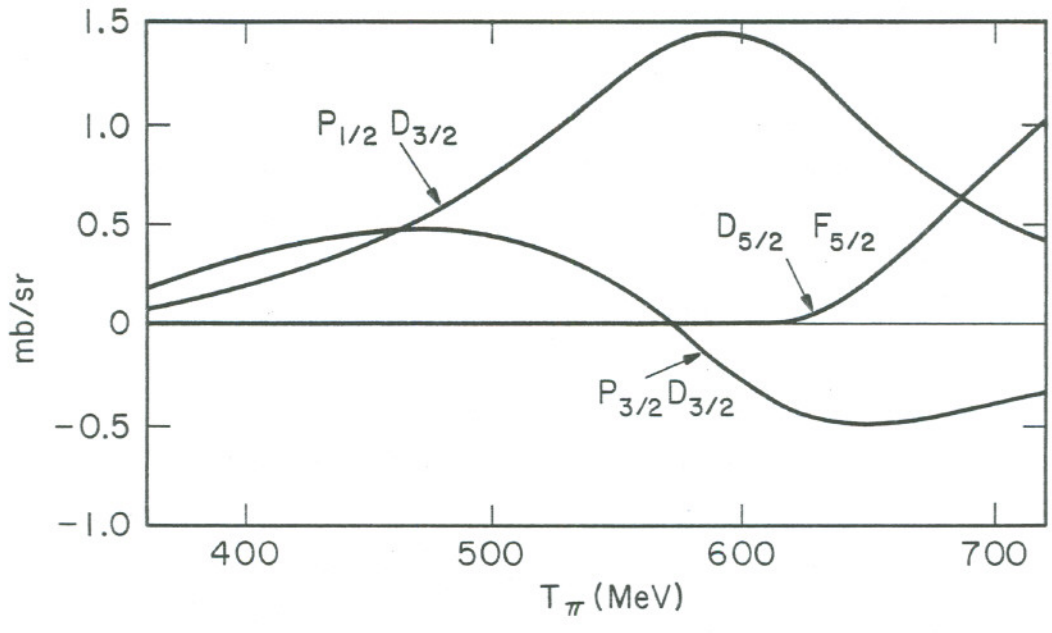

Fig. 38. Contribution to a_1 from $P_{1/2}D_{3/2}$, $P_{3/2}D_{3/2}$, and $D_{5/2}F_{5/2}$ terms.

we did for the $S_{1/2}$, that the $P_{1/2}$ amplitude is pure imaginary and constant, the $P_{1/2}D_{3/2}$ contribution to a_1 is as shown in Fig. 38. Furthermore, the $P_{1/2}D_{3/2}$ interference term does not contribute to any other coefficient.

Thus, one can see the motivation for choosing the forms of the amplitudes given in Figs. 32 and 33. Using these amplitudes and considering all the terms that contribute to each coefficient, we obtain the behavior of the coefficients shown in Figs. 39 and 40. The data of this experiment and the 698-MeV data of Helland, et al.[5a] are also plotted in Figs. 39 and 40.

One can see that the agreement between the data and the predictions is fairly good in view of the many simplifying assumptions made. This does not prove the existence of a resonance in the D_{13} state but shows that the data appear to be consistent with a D_{13} resonance.

In regard to the evidence for two resonances in the 400- to 700-MeV region, it can only be said that in this rough analysis the necessity of a second resonance was not apparent.

D. Summary

In summary, we can say that the D_{13} state rises to prominence in the energy region from 400 to 700 MeV. Furthermore, it appears that the π^--p differential-cross-section data are consistent with a D_{13} phase shift that passes through 90 deg. However, an alternative explanation cannot be ruled out. Because of the importance of inelastic processes, the D_{13} resonance, if indeed it may be called a resonance, may be of a nature fundamentally different from that of a bound-state type resonance, associated with a Regge pole. Further investigation will be necessary to resolve these uncertainties. Accurate polarization and charge-exchange measurements should aid in a better understanding of this problem.

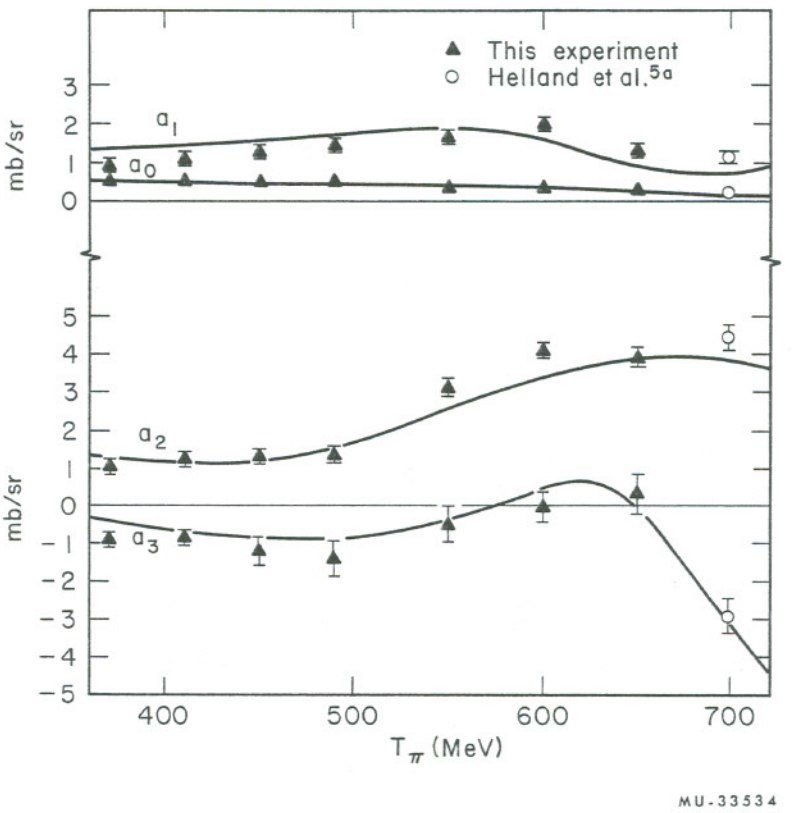

Fig. 39. Energy dependence of π^--p coefficients a_0, a_1, a_2, and a_3 using the scattering amplitudes in Figs. 32 and 33. The data are plotted again for comparison.

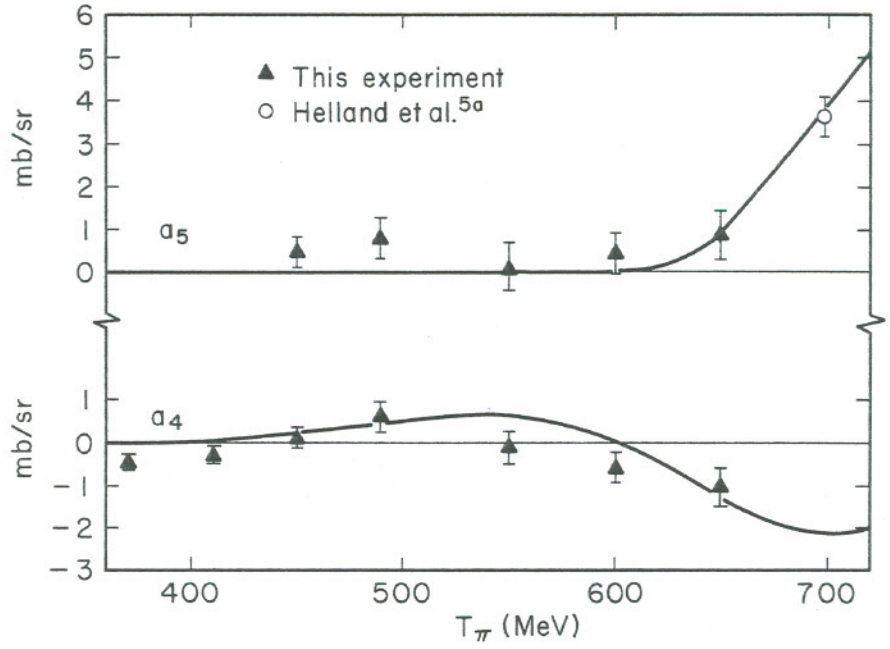

Fig. 40. Energy dependence of π^--p coefficients a_4 and a_5 using the scattering amplitudes in Figs. 32 and 33. The data are plotted again for comparison.

ACKNOWLEDGMENTS

The author is deeply indebted to Dr. Burton J. Moyer for his invaluable assistance and guidance, not only during the performance of the experiment but throughout the period of the author's graduate study.

Special thanks are also due to Dr. Jerome A. Helland for many helpful discussions and for his tireless efforts in the preparation and performance of the experiment.

Much helpful assistance in preparing and running the experiment was received from Dr. Donald E. Hagge, Dr. Jean-Francois Detoeuf, Dr. Jacques Teiger, Mr. Marcel Banner, and Mr. Jean Hamel.

The author is grateful to Dr. A. C. Helmholz for many helpful suggestions and for his interest throughout the experiment.

Special recognition should be given to Mr. Larry Scott. He was responsible for most of the special electronic circuitry.

For work in the development and testing of the electronic equipment, thanks are due to Messrs. Dick A. Mack, Frederick Kirsten, Cordon R. Kerns, Fong Gin, Robert J. Rudden, John M. Wolverton, and Alain Bissonet.

Mr. Armond Conti, Mr. Leo Leidy, and Mr. Jean Thibaud were responsible for the mechanical supports and other special equipment used in the experiment.

The author is grateful to Mr. Robert Levy-Mandel and his staff for the operation of the Saclay synchrotron.

Sincere thanks are due to Miss Miriam Machlis and several others who had a part in bringing this thesis to final form.

This work was done under the auspices of the U. S. Atomic Energy Commission and the French Commissariat a l'Energie Atomique.

REFERENCES

1. G. M. G. Lattes, H. Muirhead, G. P. S. Occhialini, and C. F. Powell, Nature 159, 694 (1947).
2. (a) W. O. Lock, High Energy Nuclear Physics (John Wiley and Sons, Inc., New York, 1960), p. 61.
   (b) A. N. Diddens, E. W. Jenkins, T. F. Kycia, and K. F. Riley, Phys. Rev. Letters 10, 262 (1963).
3. See, for example:
   J. Ashkin, J. P. Blaser, F. Feiner, and M. O. Stern, Phys. Rev. 105, 724 (1957).
4. (a) J. H. Foote, O. Chamberlain, E. H. Rogers, H. M. Steiner, C. E. Wiegand, and T. Ypsilantis, Phys. Rev. 122, 948 (1961).
   (b) J. H. Foote, O. Chamberlain, E. H. Rogers, and H. M. Steiner, Phys. Rev. 122, 959 (1961).
   (c) H. R. Rugge and O. T. Vik, Phys. Rev. 129, 2300 (1963).
   (d) O. T. Vik and H. R. Rugge, Phys. Rev. 129, 2311 (1963).
   (e) Roger Hill, Pion-Nucleon Scattering at 310 MeV: Neutron Polarization in $\pi^- + p \rightarrow \pi^0 + n$ and Phase Shift Analysis (Ph. D. Thesis), Lawrence Radiation Laboratory Report UCRL-11140 (in preparation).
5. (a) J. A. Helland, T. J. Devlin, D. E. Hagge, M. J. Longo, B. J. Moyer, and C. D. Wood, Phys. Rev. Letters 10, 27 (1963).
   (b) C. D. Wood, T. J. Devlin, J. A. Helland, M. J. Longo, B. J. Moyer, and V. Perez-Mendez, Phys. Rev. Letters 6, 481 (1961).
   (c) Richard D. Eandi, Polarization of Recoil Protons in Pion-Proton Elastic Scattering at 523, 572 and 689 MeV (Ph. D. Thesis), Lawrence Radiation Laboratory Report UCRL-10629, March 1963 (unpublished).
6. (a) M. E. Blevins, M. M. Block, and J. Leitner, Phys. Rev. 112, 1287 (1958).
   (b) R. R. Crittenden, J. H. Scandrett, W. D. Shephard, W. D. Walker, and J. Ballam, Phys. Rev. Letters 2, 121 (1959).
   (c) L. K. Goodwin, R. W. Kenney, and V. Perez-Mendez, Phys. Rev. 122, 655 (1961).

(d) F. Grard, G. MacLeod, L. Montanet, M. Cresti, R. Barloutaud, C. Choquet, J. Gaillard, J. Heughebaert, A. Leveque, P. Lehman, J. Meyer, and D. Revel, Nuovo Cimento 22, 193 (1961).

(e) E. L. Grigoryev and N. A. Mitin, Soviet Phys. JETP 10, 1123 (1960).

(f) M. Kozodaev, R. Suliaev, A. Fillipov, and Iu. Shcherbakov, Soviet Phys. Doklady 1, 171 (1956).

(g) R. S. Margulies, Phys. Rev. 100, 1255 (1955).

(h) N. A. Mitin and E. L. Grigoryev, Soviet Phys. JETP 5, 378 (1957).

(i) John I. Shonle, Phys. Rev. Letters 5, 156 (1960).

(j) William J. Willis, Phys. Rev. 116, 753 (1959).

(k) V. G. Zinov and S. M. Korenchenko, Soviet Phys. JETP 11, 794 (1960).

(l) Peter C. A. Newcomb, Phys. Rev. 132, 1283 (1963).

7. R. B. Scott and F. G. Brickwedde, J. Res. Natl. Bur. Std. 19, 237 (1937).

8. J. Duboc, J. Banaigs and J. F. Detoeuf, J. Phys. Radium 22, 64A (1961).

9. Lawrence Radiation Laboratory Counting Handbook, UCRL-3307 Rev., Jan. 1959 (unpublished).

10. Stanley L. Klezmer, Shielded Nanosecond Logic Circuits, Lawrence Radiation Laboratory Report UCID-1823, Nov. 1962 (unpublished).

11. Larry Scott, 256 Channel Coincidence Matrix, Lawrence Radiation Laboratory Report UCID-1597, Oct. 1961 (unpublished).

12. Larry Scott, Double Pulse Recognition System, Lawrence Radiation Laboratory Engineering Note EE-812, Oct. 1961 (unpublished).

13. O. A. Kerns and R. F. Tusting, Constant-Amplitude Light-Flash Generator for Gain Stabilization of Photosensitive Systems, Lawrence Radiation Laboratory Report UCRL-10895, July 1963 (unpublished).

14. R. J. Cence, D. A. Cheng, and C. B. Chiu (Lawrence Radiation Laboratory, Berkeley, California) private communication.
15. P. Cziffra and M. J. Moravcsik, A Practical Guide to the Method of Least-Squares, Lawrence Radiation Laboratory Report UCRL-8523 Rev., June 1959 (unpublished).
16. Ronald F. Peierls, Phys. Rev. 118, 325 (1960).
17. P. Bareyre, C. Bricman, G. Valladas, G. Villet, J. Bizard and J. Sequinot, Phys. Letters 8, 137 (1964).
18. L. David Roper (Lawrence Radiation Laboratory, Livermore, California) private communication.
19. P. Carruthers, Phys. Rev. Letters 10, 540 (1963).
20. J. S. Ball and W. R. Frazer, Phys. Rev. Letters 7, 204 (1961).
21. Howard J. Schnitzer, Phys. Rev. 125, 1059 (1962).
22. Richard J. Kurz, Differential Distributions of Neutrons in Inelastic $\pi^- p$ Interactions at 374, 417, and 454 MeV (Ph. D. Thesis), Lawrence Radiation Laboratory Report UCRL-10564, Nov. 1962 (unpublished).
23. J. Kirz, J. Schwartz, and R. D. Tripp, Phys. Rev. 130, 2481 (1963).
24. J. M. Blatt and V. F. Weisskopf, Theoretical Nuclear Physics (John Wiley and Sons, Inc., New York, 1952), p. 400.
25. M. B. Watson, M. Ferro-Luzzi, and R. D. Tripp, Phys. Rev. 131, 2248 (1963).
26. R. Omnes and G. Valladas, Proc. of Int. Conf. on Elementary Particles, Aix en Provence, Sept. 1961, Vol. I, p. 467.